Published OnlineFirst May 21, 2013; DOI: 10.1158/0008-5472.CAN-12-3837

Cancer Research

Manganese-Enhanced MRI Reveals Early-Phase Radiation-Induced Cell Alterations *In Vivo*

Shigeyoshi Saito, Sumitaka Hasegawa, Aiko Sekita, et al.

Cancer Res 2013;73:3216-3224. Published OnlineFirst May 21, 2013.

Published OnlineFirst May 21, 2013; DOI: 10.1158/0008-5472.CAN-12-3837

Integrated Systems and Technologies

Cancer Research

Manganese-Enhanced MRI Reveals Early-Phase Radiation-Induced Cell Alterations *In Vivo*

Shigeyoshi Saito[1,2], Sumitaka Hasegawa[2], Aiko Sekita[2], Rumiana Bakalova[2], Takako Furukawa[2], Kenya Murase[1], Tsuneo Saga[2], and Ichio Aoki[2]

Abstract

For tumor radiotherapy, the *in vivo* detection of early cellular responses is important for predicting therapeutic efficacy. Mn^{2+} is used as a positive contrast agent in manganese-enhanced MRI (MEMRI) and is expected to behave as a mimic of Ca^{2+} in many biologic systems. We conducted *in vitro* and *in vivo* MRI experiments with Mn^{2+} to investigate whether MEMRI can be used to detect cell alterations as an early-phase tumor response after radiotherapy. Colon-26 cells or a subcutaneously grafted colon-26 tumor model were irradiated with 20 Gy of X-rays. One day after irradiation, a significant augmentation of G_2–M-phase cells, indicating a cell-cycle arrest, was observed in the irradiated cells in comparison with the control cells, although both early and late apoptotic alterations were rarely observed. The MEMRI signal in radiation-exposed tumor cells (R_1: 0.77 ± 0.01 s^{-1}) was significantly lower than that in control cells (R_1: 0.82 ± 0.01 s^{-1}) *in vitro*. MEMRI signal reduction was also observed in the *in vivo* tumor model 24 hours after irradiation (R_1 of radiation: 0.97 ± 0.02 s^{-1}, control: 1.10 ± 0.02 s^{-1}), along with cell-cycle and proliferation alterations identified with immunostaining (cyclin D1 and Ki-67). Therefore, MEMRI after tumor radiotherapy was successfully used to detect cell alterations as an early-phase cellular response *in vitro* and *in vivo*. *Cancer Res; 73(11); 3216–24. ©2013 AACR.*

Introduction

Radiotherapy involves the use of high-energy X-rays or charged particles to treat malignancies with the intention of destroying or inactivating cancer cells while preserving normal tissue integrity (1–4). Many types of biomarkers are used to detect cell viability and responses after radiotherapy *in vitro*. Although cell apoptosis is an important marker, apoptosis after radiation is observed only in limited cell types, such as hematopoietic and germ cells. In addition, radiation exposure immediately induces a significant G_2 cell-cycle arrest in many types of tumor cells (5), as well as prolonged G_1 cell-cycle arrest in normal fibroblast and ependymal cells (6, 7). The appearance ratio of the cell-cycle arrest linearly correlates with the radiation dose and cell viability in both normal and tumor cells (8). In addition, radiation-induced cell-cycle arrest can be linked to irreversible growth arrest, such as senescence-like growth arrest (SLGA), which is associated with the expression of senescence-associated β-galactosidase (SA-β-gal; ref. 9). Thus, cell-cycle arrest and alteration can be an early biomarker for evaluating therapeutic efficiency immediately after radiotherapy.

The divalent manganese ion (Mn^{2+}) has long been known as a positive intracellular MRI contrast agent because of its ability to alter the longitudinal relaxation of water protons. Manganese-enhanced MRI (MEMRI) provides a unique opportunity to study neuronal activation and architecture (10–12). The underlying principle of MEMRI lies in the fact that Mn^{2+} behaves in a manner similar to the calcium ion (Ca^{2+}) in many biologic systems (13). Extracellular Mn^{2+} can enter cells through *N*-methyl-D-aspartate (NMDA) receptors for glutamate (14) and/or voltage-gated calcium channels (15). Previous studies have found that MEMRI is useful for the *in vivo* visualization of tumors such as those arising from head and neck region (16, 17). There are several reports, discussing the factors associated with Mn enhancement and tumor uptake. The tumor cell uptake of Mn^{2+} is linked to the proliferation rate *in vitro* of human tumor cells (18). In addition, Mn^{2+} is considered to be a cell viability indicator in myocardial infarction (19, 20). Therefore, it is possible that radiation-induced cell-cycle alteration and the associated suppression of cell proliferation can be detected from the alterations in MEMRI signal enhancement.

The goal of this study was to test the hypothesis that MEMRI can be used to detect radiation-induced alterations as an early-phase tumor response after radiotherapy. In this study, we evaluated Mn^{2+} uptake in a colon cancer cell line and a

Authors' Affiliations: [1]Department of Medical Physics and Engineering, Division of Medical Technology and Science, Faculty of Health Science, Graduate School of Medicine, Osaka University, Osaka and [2]Molecular Imaging Center, National Institute of Radiological Sciences, Chiba, Japan

Note: Supplementary data for this article are available at Cancer Research Online (http://cancerres.aacrjournals.org/).

Corresponding Author: Ichio Aoki, Molecular Imaging Center, National Institute of Radiological Sciences, Molecular Imaging Building 3F, Anagawa 4-9-1, Inage, Chiba 263-8555, Japan. Phone: 81-43-206-3272; Fax: 81-43-206-3276; E-mail: aoki@nirs.go.jp

doi: 10.1158/0008-5472.CAN-12-3837

Published OnlineFirst May 21, 2013; DOI: 10.1158/0008-5472.CAN-12-3837

subcutaneous grafted mouse model by *in vitro/in vivo* MEMRI after X-ray exposure (20 Gy).

Materials and Methods

Colon cancer cells and *in vitro* irradiation experiment

The murine colon cancer cell line (colon-26) was maintained in Dulbecco's Modified Eagle Medium (DMEM; Sigma-Aldrich Japan) supplemented with 10% fetal calf serum (Nichirei) and 1% penicillin–streptomycin (Invitrogen Japan K.K.). Cells were cultured under high humidity with 5% CO_2 at 37°C. After incubation for 4 days, the colon-26 cells underwent a single exposure to X-rays at a dose of 20 Gy. The X-ray exposure conditions were: peak voltage of 200 kV, current of 20 mA, filter consisting of 0.5 mm Cu + 0.5 mm Al, a distance between the focus and objective of 550 mm and a dose rate of 1.2 to 1.3 Gy/min. The radiation dose and colon-26 cell type were selected as a "less apoptotic model" based on the evidence described in a previous report (21).

In vitro Mn^{2+} uptake study by MRI

We prepared 6 colon-26 cell pellets (control group, 3; radiation exposure group, 3) for MRI experiments at 24 hours after irradiation. The *in vitro* MRI acquisitions were carried out using a 7-T, 40 cm bore MRI magnet (Kobelco and Jastec) interfaced with a Bruker console (BioSpec, Bruker Biospin). A birdcage coil (38 mm inner diameter, transmission and reception; Rapid Biomedical) was used for the measurement of tumor cell samples. The samples were maintained at approximately 23°C.

Manganese chloride ($MnCl_2$; $MnCl_2$-$4H_2O$, Sigma-Aldrich Japan) was dissolved in the DMEM at a concentration of 0.1 mmol/L. The cells were incubated in the medium, either with or without $MnCl_2$, for 30 minutes at 37°C under 5% CO_2. After incubation, the medium was carefully removed by washing twice with PBS. The cells were harvested and dissociated with trypsin, transferred to PCR tubes, and cell pellets were collected by centrifugation. For the T_1-weighted image (T_1WI), a 2-dimensional (2D), single-slice image was obtained using a conventional spin echo (SE) sequence with the following parameters: repetition time (TR) = 350 ms, echo time (TE) = 9.57 ms, matrix size = 256 × 256, field of view (FOV) = 40.0 × 40.0 mm^2, slice thickness (ST) = 1.0 mm, fat suppression preparation (Fat-Sup) = on, number of acquisitions (NA) = 8, and slice orientation = sagittal. For this imaging sequence, the nominal voxel resolution was 156 × 156 × 1,000 μm^3. The total acquisition time for the T_1WI was 11 minutes and 56 seconds. For the inversion recovery, 2D, single-slice inversion recovery MRI was carried out using rapid acquisition with relaxation enhancement (RARE) acquisition for the T_1 map calculation with the following parameters: TR = 10,000 ms; TE = 10 ms; inversion time = 51, 100, 200, 400, 800, 1,600, 3,200, or 6,400 ms; matrix size = 256 × 256; slice orientation = sagittal (same slice orientation as that used for the T_1WI); FOV = 40.0 × 40.0 mm^2; ST = 1.0 mm; Fat-Sup = on; RARE factor = 4; and NA = 1. For this image, the nominal voxel resolution was 156 × 156 × 1,000 μm^3. The total acquisition time for inversion recovery MRI was 49 minutes and 27 seconds. The quantitative T_1 maps were calculated by conducting nonlinear least squares fitting using inversion-recovery MRI. Regions of interest (ROI) were defined on pelleted cell regions. The R_1 values in the ROI were calculated as the inverses of the T_1 values. All calculations and analyses were carried out using the MRVision image analysis software (Version 1.5.8, MRVision Co.).

Flow cytometry for cell viability and cell-cycle assays

Cell apoptosis and cycle alterations were measured using Guava Viacount and Guava Cell Cycle Reagents (Guava Technologies Inc.), followed by analysis of the cells using a Guava PCA machine (Guava Technologies Inc.). Cells were placed in 4 plates and adhered overnight for 24 hours after radiation exposure. Cells were stained with Guava Viacount and Cell Cycle Reagents according to the manufacturer's instructions.

In vivo animal model and radiation exposure

The Animal Welfare Committee of our Institution approved all studies. Male BALB/c nu/nu mice (n = 17, 21.3 ± 1.4 g, 8 weeks old; Japan SLC) were rested for 1 week before the experiment. The animals had free access to food and water and were kept under standard laboratory conditions in a specific pathogen-free environment, at 22°C to 23°C, with approximately 50% humidity, and a 12:12-hour light/dark cycle. Colon-26 cells (1×10^7) were injected subcutaneously into both legs of the male BALB/c nu/nu mice. Seven days after the injection, the tumor-bearing mice were subjected to MRI and histologic experiments. All mice underwent a single X-ray exposure of the left leg (the right legs were covered by a 1 cm thick lead layer) at a dose of 20 Gy on day 7 after inoculation of colon-26 cells. The X-ray exposure conditions were as follows: peak voltage of 200 kV, current of 20 mA, filter consisting of 0.5 mm Cu + 0.5 mm Al, a distance between the focus and objective of 550 mm, and a dose rate of 1.2 to 1.3 Gy/min. The male BALB/c nu/nu mice were divided into 2 groups (for MRI study, n = 10; for tumor growth study, n = 7). Following the radiation exposure, all mice, both control and radiation exposed, were maintained under 12:12 hour light/dark cycles until the MRI and tumor growth experiment.

In vivo MRI study

The mice were anesthetized with 2.0% isoflurane and placed in the prone position; the anesthesia was maintained at this level for MRI scanning. During the experiment, a warm flow of air over the animal maintained the body temperature at 37.0°C. The respiratory rate was maintained and monitored throughout the experiment using a rodent ventilator (MRI-1, CWE, Inc.). Before the T_1WI acquisitions, scout images were acquired, and quantitative T_2 mapping was carried out to localize the tumor. T_2 mapping was done for the assessment of necrosis in the tumors using a multi-slice, multi-echo SE sequence (TR = 3,000 ms, slice thickness = 1 mm, FOV = 40.0 × 40.0 mm, matrix = 256 × 256, slice orientation = transaxial, number of repetitions = 1), with echo times ranging from 10 to 140 ms in steps of 10 milliseconds. The total acquisition time was 10 minutes and 20 seconds.

T_1WI acquisition and quantitative T_1 mapping were carried out in the following order: preadministration (control), gadolinium (Gd)-enhanced, and Mn-enhanced experiments. First,

Published OnlineFirst May 21, 2013; DOI: 10.1158/0008-5472.CAN-12-3837

one set of T_1WIs and a T_1 map were acquired as baseline data before the administration of Gd. Second, the T_1WI and T_1 map acquisition set was repeated 4 times every 16 minutes after the administration of gadopentetate dimeglumine (Gd-DTPA). Gd-DTPA (150 μmol/kg; Bayer Japan) was diluted to a concentration of 50 mmol/L with saline and injected intravenously to evaluate tumor vasculature. A waiting time of 90 minutes was included after the first and second steps to avoid potential Gd retention in tumors. Before the administration of $MnCl_2$, we confirmed that the Gd-DTPA–related signal had returned to the baseline level. Third, T_1WI and T_1 map acquisition sets were repeated 4 times every 16 minutes after starting the Mn infusion. Before the administration, 100 mmol/L $MnCl_2$ ($MnCl_2$-$4H_2O$, Sigma-Aldrich Japan) was dissolved in distilled water and diluted to 50 mmol/L with saline to match the osmotic pressure of blood. We slowly infused the 50 mmol/L, osmotic pressure-controlled $MnCl_2$ solution (380 μmol/kg) at a rate of 0.4 mL/h through the tail vein using a syringe pump (KDS-100, KD scientific, Inc.). In subcutaneous tumors, a 2D, single-slice T_1WI was obtained using a conventional SE sequence with the following parameters: TR = 350 ms, TE = 9.57 ms, matrix size = 256 × 256, FOV = 40.0 × 40.0 mm^2, ST = 1.0 mm, Fat-Sup = on, and NA = 4. The slice orientation was transverse. For these images, the nominal voxel resolution was 156 × 156 × 1,000 μm^3. The total acquisition time was 5 minutes and 7 seconds. T_1 mapping was carried out with a single-slice 2D Look-Locker sequence (TR = 10,000 ms, TE = 10 ms, ST = 1.0 mm, matrix size = 128 × 64, FOV = 25.6 × 12.8 mm^2, NA = 1) and acquired over a period of 10 minutes and 40 seconds. For ROI studies, the first image set of 4 Gd-DTPA administration sets and third image set of 4 Mn administration sets were used. The ROIs of the subcutaneous tumor core and peripheral area were defined by the following methods. The outlines of the ROIs (ROI_{out}) were manually delineated on the T_1WI. Gd-enhanced areas over the threshold level (+2 SDs of the mean signal intensity of the ROI_{out} in the control image) were then defined as the peripheral areas using first image set after Gd-DTPA injection. The peripheral areas were excluded from the ROI_{out}. The areas that excluded the peripheral areas from the ROI_{out} were defined as the tumor core areas.

Histology

All tumors were studied histologically to clarify the source of the T_1 change. Mice were euthanized by pentobarbital (1.0 mL/animal; Dainippon-Sumitomo Pharmaceutical) overdose after the MRI scans and were prepared for histology by transcardiac perfusion with saline-containing heparin followed by 4% paraformaldehyde (Otsuka Pharmaceutical Co., Ltd.). Tissues were embedded in paraffin and transaxially sectioned into 4 μm thick sections, which were then placed on slides at the locations and orientations corresponding to the MRI slices. The slides were processed for cyclin D1 (Nichirei Biosciences Inc.), Ki-67 (Dako Japan Inc.), and activated caspase-3 (Cell Signaling Technology Japan) staining. After visualization with diaminobenzidine (DAB; DAKO Japan Inc.), tissue sections were briefly counterstained with hematoxylin. Three types of staining were conducted for each tumor. Cyclin D1 (for the detection of cell-cycle alterations) and Ki-67 (for the assessment of tumor proliferation) were identified as follows; (i) the brightness and contrast were automatically optimized using Photoshop (Ver. 8.0.1, Adobe, Inc.); (ii) the brown-stained positive cells were enhanced and converted to a black and white binary map using the "Make binary" plug-in of ImageJ (Ver.1.40g, NIH); (iii) the total area of the black regions of the binary map was measured using the "ROI" and "Measure" plug-ins of ImageJ; (iv) the ratio of the positive cell area to the total area was calculated. To identify cells that underwent apoptosis as a result of radiation exposure, the number of positive cells per square millimeter of tumor was calculated in the activated caspase-3–stained slices.

Tumor growth study

In 7 tumor-bearing mice, 2 perpendicular tumor diameters were measured with a caliper on days 1, 3, and 7 after radiation exposure. The tumor volumes were calculated as $V = (\pi/6) \times a$ (mm) $\times b^2$ (mm^2), where a and b are the largest and smallest perpendicular tumor diameters, respectively. Subsequent measurements were normalized to the pretreatment tumor volume.

Statistical analysis

The data are presented as the mean ± SD. All statistical analyses were conducted using Prism 5 (Version 5.0, GraphPad Software, Inc.). Longitudinal relaxation rates ($R_1 = 1/T_1$) before and after $MnCl_2$ administration in the control and radiation-exposed tumors were calculated. We compared control and radiation-exposed groups using the unpaired t test and considered values of $P < 0.05$ to be significant for the *in vitro* Mn-uptake study, tumor size analysis, *in vivo* T_2 quantitative MRI data analysis, and histologic experiments. A one-way ANOVA with Tukey *post hoc* test was applied to compare R_1 values between tumors.

Results

In vitro imaging of tumor cells using MEMRI

Figure 1A shows T_1-weighted MR images of the pellets of colon-26 cells, either exposed or not exposed to radiation, after incubation in a standard medium with or without 0.1 mmol/L $MnCl_2$ supplementation. Irradiated colon-26 cells showed less signal enhancement compared with control colon-26 cells after $MnCl_2$ administration at 24 hours after X-ray irradiation (Fig. 1A). The R_1 values in the irradiated colon-26 cells (0.77 ± 0.01 s^{-1}) were lower than those in the control colon-26 cells (0.82 ± 0.01 s^{-1}) when loaded with 0.1 mmol/L $MnCl_2$ (Fig. 1B; **, $P < 0.01$).

Flow cytometry for the assessment of cell cycle and viability

Figure 2A and B show the results of the flow cytometric cell-cycle analysis. The proportion of G_2–M-phase cells was increased in the radiation-exposed samples (G_2–M of 34.9%; Fig. 2B) in comparison with the control cells (G_2–M of 28.4%; Fig. 2A). Moreover, the proportion of G_0–G_1 phase cells was markedly decreased in the radiation-exposed samples

Published OnlineFirst May 21, 2013; DOI: 10.1158/0008-5472.CAN-12-3837

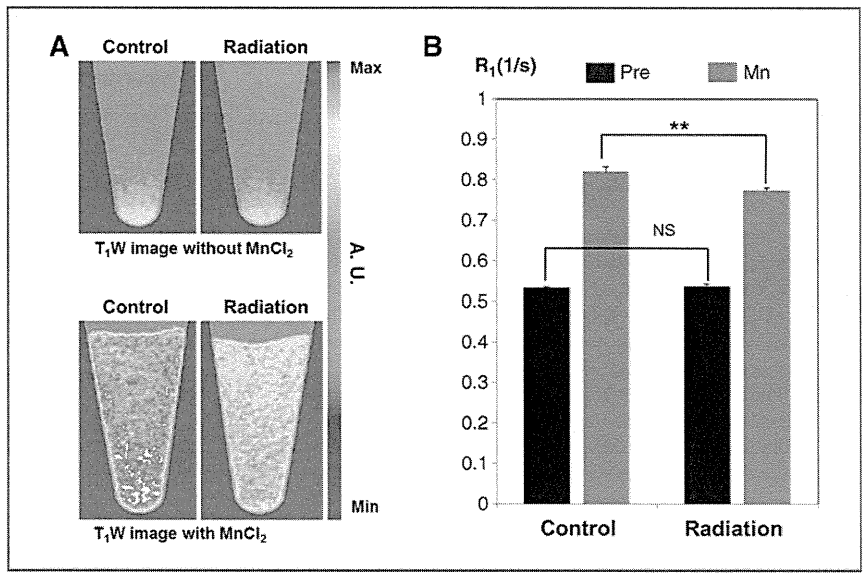

Figure 1. *In vitro* imaging of tumor cells using MEMRI. A, T_1 weighted images of the colon-26 cell pellets with (left) or without (right) X-ray exposure incubated with (top) or without (bottom) 0.1 mmol/L $MnCl_2$. The signal from the control colon-26 cells was enhanced by $MnCl_2$ in comparison with the X-ray–exposed colon-26 cells (top, control). The signal intensity is indicated by the color bar (arbitrary unit). B, R_1 values of the cells. The R_1 values in the X-ray–exposed colon-26 cells were lower than those in the control colon-26 cells when loaded with 0.1 mmol/L $MnCl_2$ (**, $P < 0.01$).

(G_0–G_1 of 1.3%; Fig. 2B) in comparison with the control cells (G_0–G_1 of 22.1%; Fig. 2A). Figure 2C and D show the results of the flow cytometric apoptosis analysis. More apoptotic cells were detected in the radiation-exposed samples (16.8%; Fig. 2D, bottom right, black arrow) in comparison with the control cells (7.1%;Fig. 2C, bottom right).

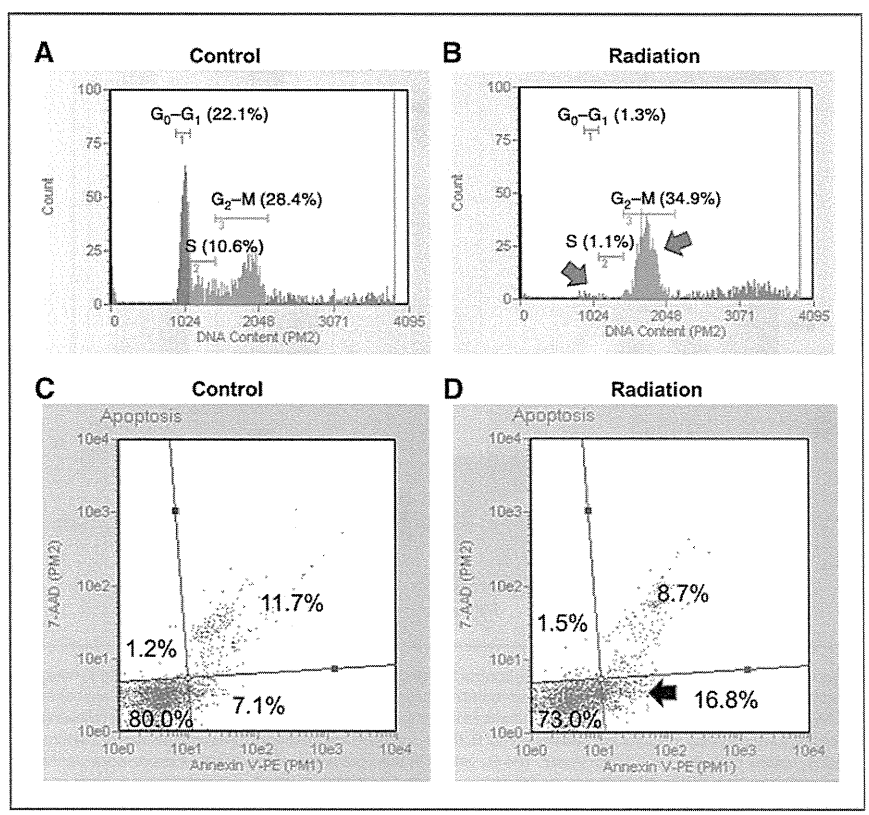

Figure 2. Cell-cycle and cell viability analyses using flow cytometry. A and B, flow cytometric cell-cycle analysis. The proportion of G_2-phase cells was increased in the radiation-exposed samples in comparison with the control samples (red arrow). Moreover, the number of G_0–G_1 phase cells was decreased in the radiation-exposed samples in comparison with the control samples (green arrow). C and D, flow cytometric apoptosis analysis. A greater number of apoptotic cells were detected in the radiation-exposed samples (black arrow) in comparison with the control samples.

Published OnlineFirst May 21, 2013; DOI: 10.1158/0008-5472.CAN-12-3837

Tumor growth

The tumor size ratio with respect to the pretreatment size is shown in Fig. 3 for both groups. There was no significant difference between the tumor sizes of 2 groups 1 day after radiation exposure, although the volume of the irradiated tumor was significantly smaller than that of the control groups on the third and seventh days ($P < 0.001$).

In vivo tumor imaging using MEMRI

We used Gd-DTPA to evaluate tumor vasculature condition and exclude the area where Gd-DTPA was highly accumulated because of disruption of the intratumor microvasculature. The core areas of control and radiation-exposed tumors were homogeneously and almost equally enhanced by Gd-DTPA (Fig. 4A). After disappearance of the Gd-enhancement (typically within 60 minutes), we obtained MEMRI with systemic $MnCl_2$ administration. In contrast to Gd-enhanced MRI, the control tumors were preferentially enhanced by $MnCl_2$ in the

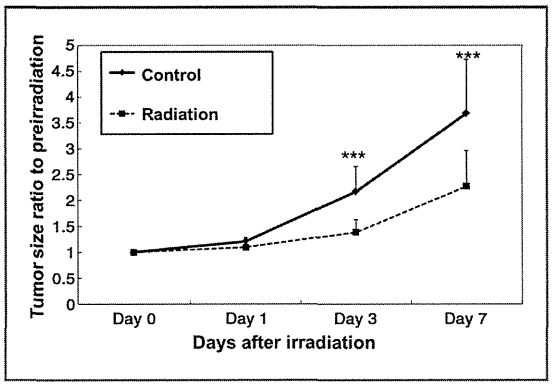

Figure 3. Tumor volume measurements. Tumor growth was significantly retarded in the radiation-exposed group after 3 and 7 days (***, $P < 0.001$). There was no significant difference between the tumor sizes of 2 groups 1 day after treatment.

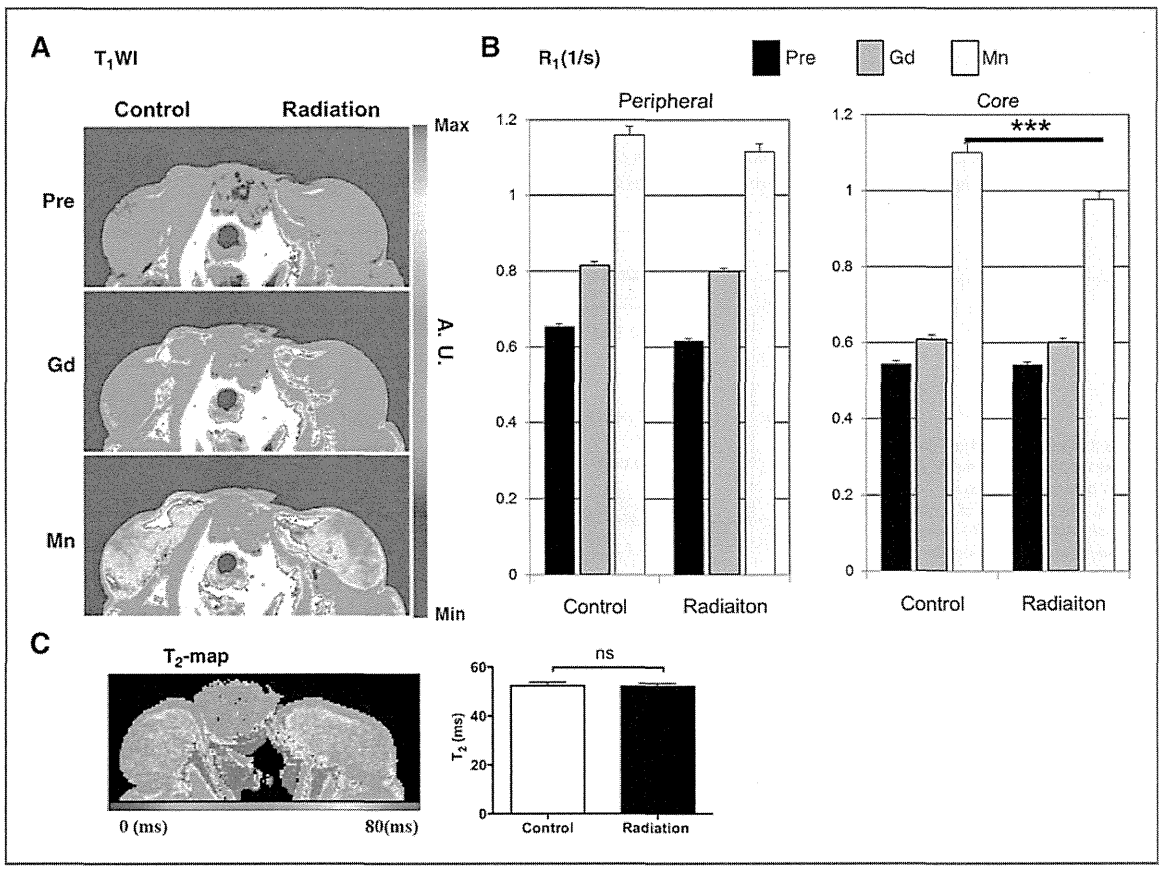

Figure 4. *In vivo* imaging using MEMRI. A, top, control T_1-weighted image. A, middle, Gd-enhanced first T_1-weighted image. A, bottom, Mn-enhanced third T_1-weighted image. The core areas of control and radiation-exposed tumors were homogeneously and almost equally enhanced by Gd-DTPA (A, middle). In MEMRI, the control tumor was preferentially enhanced in comparison with the radiation-exposed tumor following $MnCl_2$ administration (A, bottom). The signal intensity is indicated by the color bar (arbitrary unit). B, the R_1 values in the peripheral area and the core of the tumors. There are no differences in the peripheral area R_1 values between the 2 tumor types. The R_1 values in the core areas of the control tumors were significantly higher at 30 minutes after Mn^{2+} administration than that in the radiation-exposed tumors (***, $P < 0.001$). C, the T_2-map of the X-ray–treated and control tumors. There are no differences between both tumor T_2 values.

Published OnlineFirst May 21, 2013; DOI: 10.1158/0008-5472.CAN-12-3837

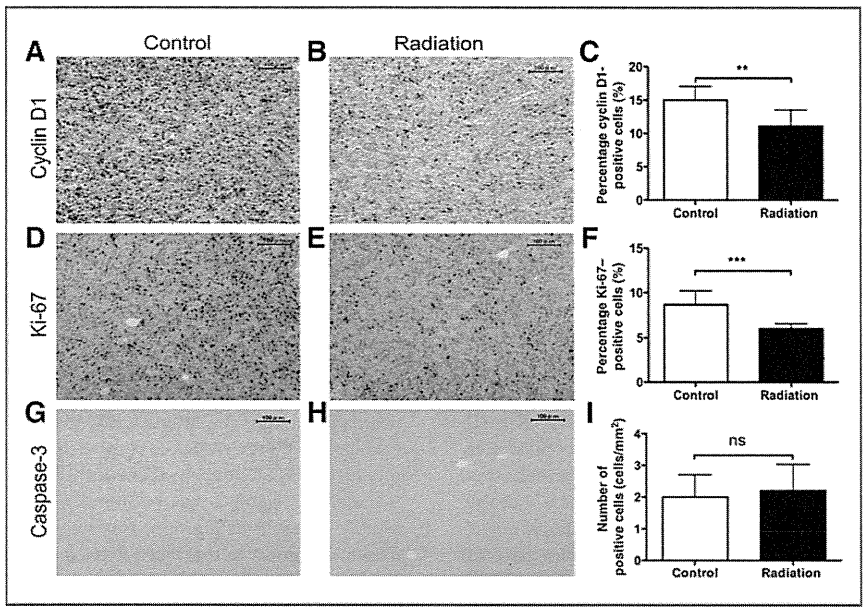

Figure 5. Immunohistochemical staining of tumors. A, cyclin D1 staining of the control tumor core region. B, cyclin D1 staining of the radiation-exposed tumor core region. C, statistical analysis of cyclin D1-positive cells. D, Ki-67 staining of the control tumor core regions. E, Ki-67 staining of the radiation-exposed tumor core regions. F, statistical analysis of Ki-67–positive cells. G, activated caspase-3 staining of the control tumor core regions. H, activated caspase-3 staining of the radiation-exposed tumor core regions. I, statistical analysis of the activated caspase-3–positive cells. These immunohistologic staining results show the detection of cellular alterations in the tumor core at 24 hours following radiation exposure. The number of positively stained cells in the core was decreased for cyclin-D1 (C) and Ki-67 (D vs. E) in exposed colon-26 tumors. The number of Ki-67–positive cells was decreased at 24 hours after radiation exposure (F). However, the number of apoptotic cells was not significantly different between the radiation-exposed and control tumors (I). Magnification, ×200; the black bar on the right represents 100 μm. (**, $P < 0.01$; ***, $P < 0.001$).

T_1WI in comparison with the radiation-exposed tumors (Fig. 4A). Figure 4B shows the R_1 values in the peripheral and core areas of the tumors. There were no differences in the tumor R_1 values in the peripheral areas between the 2 tumor types (Fig. 4B; peripheral: control, $0.61 \pm 0.01\ s^{-1}$ and radiation-exposed, $0.60 \pm 0.01\ s^{-1}$). However, the R_1 values in the core areas of the control tumor were significantly higher at 30 minutes following Mn^{2+} administration in comparison with those of the radiation-exposed tumors (Fig. 4B; core, $P < 0.001$; control, $1.10 \pm 0.02\ s^{-1}$ and radiation-exposed, $0.97 \pm 0.02\ s^{-1}$). T_2 maps of the radiation-exposed and control tumors were calculated (control, 52.3 ± 1.5 ms; radiation-exposed, 52.1 ± 1.2 ms). There were no differences between the T_2 values of the tumors (Fig. 4C).

Immunohistochemical staining of tumors

Figure 5A–I shows the results of the immunohistochemical staining for the evaluation of cellular alterations in the tumor core 24 hours after radiation exposure. The immunohistologic stainings for cyclin D1 and Ki-67 indicated that both cell cycle and proliferation in the radiation-exposed tumor core were significantly changed (Fig. 5C; cyclin D1, $P < 0.01$: control, $14.9 \pm 2.0\%$ and radiation-exposed, $11.0 \pm 2.4\%$, $P < 0.01$; and Fig. 5F; Ki-67: control, $8.6 \pm 1.6\%$ and radiation-exposed, $5.9 \pm 0.6\%$, $P < 0.001$). On the other hand, the number of apoptotic cells per section was not significantly different between the radiation-exposed and control tumors (Fig. 5I, control: 2.0 ± 0.7 and radiation exposed: 2.2 ± 0.8).

Discussion

Relationship between radiation-induced cell-cycle alteration and Mn^{2+} uptake

Ca^{2+} is required to maintain normal structure and function in all living cells (22) and participates in a variety of physiologic and biologic events such as proliferation and apoptosis (23). *In vitro* calcium imaging is a common technique frequently carried out in studies that are designed to show the Ca^{2+} status of a tissue or a medium. In particular, the dynamics of intracellular Ca^{2+} can only be analyzed by optical methods using calcium-sensitive dyes for the detection of Ca^{2+}-bound fluorescence *in vitro* (24). Recently, *in vivo* MEMRI has provided a unique opportunity to study neuronal activation and architecture due to the ability of Mn^{2+} as a calcium surrogate (10–12). Mn^{2+} can enter cells via the same transport systems as those used by Ca^{2+} and can bind to a number of intracellular structures with high-affinity Ca^{2+}- and Mg^{2+}-binding sites on proteins and nucleic acids (25). Mn^{2+} as a positive contrast agent in T_1W MRI has long been used in many biologic applications for brain mapping (26), brain disease (12) (27), neuronal tract tracing (28), and cardiac functional studies (29).

Published OnlineFirst May 21, 2013; DOI: 10.1158/0008-5472.CAN-12-3837

Although several factors influencing Mn^{2+} uptake in cells have been reported such as voltage-gated Ca^{2+}-channel activities (30–33), NMDA (14) and calcium-sensing receptor (34) expression, astroglia (27) and microglia (35) activity/cellularity, activities of enzymes (e.g., manganese superoxide dismutase; refs. 36, 37) and metal transporters, the mechanisms involved in Mn^{2+} uptake in tumor cells are not well known. Some previous studies have shown that MEMRI can enhance some types of tumors *in vivo*, such as salivary gland and eye (choroidal) tumors (16, 17). In particular, Braun and colleagues showed that the uptake of Mn^{2+} by tumors depends on the cell-proliferation rate (18). Thus, we conducted a $MnCl_2$ loading study to investigate whether Mn^{2+} is accumulated in tumor cells that have undergone G_2–M cell-cycle arrest due to radiation exposure. Mn^{2+} accumulation was decreased in radiation-exposed tumor cells both *in vitro* and *in vivo* (Fig. 1B and Fig. 4A) with cell-cycle alteration as early as 24 hours after irradiation, when insignificant increase in apoptotic cells was observed (Fig. 2D and Fig. 5C). These results suggest that the cell-cycle alteration of tumor cells is an important determinant of the uptake of Mn2+ in MEMRI, and that the apoptosis of tumor cells is not a predominant factor in the decrease of Mn2+ uptake for our the 20-Gy radiation condition. At most, less than 10% increment in the number of apoptotic cells may induce a small signal reduction.

Intracellular free Ca^{2+} has been proposed to play a role in the regulation of the cell cycle (38) and in the progression into mitosis from the G_2 arrest point (39). In the late G_2 phase, cells with activated cdc2 kinase can enter into mitosis (40). However, radiation exposure induces a significant G_2 cell-cycle arrest (5, 41) and decreased functioning of cdc2 kinase (41). The local transient increase in free Ca^{2+} influences the rate of cdc2 kinase activation, and it is necessary to initiate pathways leading to cdc2 kinase inactivation in the mitotic cell cycle (42). Therefore, we suggest that the decrease in Ca^{2+} uptake due to inactivated cdc2 kinase contributes to MEMRI signal reduction in the radiation-exposed model.

Factors involved in Mn^{2+} uptake in radiation-exposed tumor cells

Other factors can alter the uptake of the Mn^{2+} contrast agent in tumor cells. For example, cell viability (apoptotic or necrotic change) and density affect Mn^{2+} uptake in MEMRI. Hu and colleagues showed that Mn^{2+} acts as a viability marker depending on Ca^{2+}-channel activity in myocardial ischemia (29). This result suggests that living cells can accumulate higher amount of Mn^{2+} than infracted cells. In our study, neither apoptosis nor necrosis was detected in the *in vivo* radiation-exposed or control tumors (Figs. 4C and 5I). In addition, exclusion of apoptotic cells from radiation-exposed tumor cells using a cell sorter did not strongly affect the MRI signal in comparison with that from non-sorted irradiated cells *in vitro* (Supplementary Fig. S1). In contrast, cell-cycle alterations were clearly detected in both *in vitro* and *in vivo* irradiated tumor cells using flow cytometry (Fig. 2) and cyclin D1 staining (Figs. 2 and 5C). Although apoptosis and apoptotic stimuli are linked to cell-cycle regulators (43), under the condition of our radiation dose and tumor model, apoptosis-altered cells did not significantly affect the MRI signal because the number of apoptotic cells was comparatively small.

In previous work, it was reported that Mn^{2+} uptake in the tumor is linked to the proliferation rate of tumor cells (18). In our study, the number of Ki-67–positive cells (potential marker of tumor growth activity; refs. 44, 45) and the MEMRI signal were decreased at 24 hours after irradiation (Fig. 5F). The Ki-67 (Fig. 5) and MEMRI observations agreed well with a previous report (18) and suggested that the Mn^{2+} accumulation in tumors, when evaluated during the early phase (24 hours) after irradiation, reflects cell-cycle alteration and a subsequent decrease in cell proliferation rather than apoptotic alterations.

Tumor vascularization is an important factor that affects the uptake of contrast agents in tumor-bearing animals. We evaluated vasculature conditions inside the tumor using an extracellular Gd-DTPA contrast agent before all MEMRI experiments (Gd-DTPA does not affect the MEMRI signal because the extracellular agent is not accumulated in the tumor and is rapidly excreted within approximately 1 hour after administration). In most cases, there was no regional enhancement inside tumors, either with or without radiation exposure, after Gd-DTPA administration (Fig. 4A). In addition, dynamic contrast-enhanced MRI (Supplementary Fig. *S2*; tumor microcirculation) and CD-31 immunohistologic staining (Supplementary Fig. *S4*; structure of vascular endothelial cells) showed that there was no significant difference in the vessel structure between the control and radiation-exposed tumors. Therefore, the 20-Gy radiation exposure for the colon-26 tumor cells did not damage the microvessel structure at 1 day *in vivo*. Consequently, it is thought that vasculature disruption in the tumor did not affect the MEMRI signal at 1 day in our model. In addition, necrotic or inflammatory alterations and bleeding in the tumors were not observed based on the T_2 values (Fig. 4C) and hematoxylin and eosin (H&E) staining (Supplementary Fig. *S3*).

In conclusion, we used MEMRI to observe the Mn^{2+} uptake in X-ray–exposed models of *in vitro* tumor cells and an *in vivo* tumor-bearing animal model. The irradiated colon-26 tumor cells underwent cell-cycle alterations (leading to decreased proliferation) but did not exhibit serious apoptotic/necrotic/inflammatory alterations or vascular damage early after irradiation. MEMRI and quantitative maps of the relaxation rate (R_1) map showed a significant signal reduction both *in vitro* and *in vivo*. Our data provides evidence that MEMRI will be a useful tool for the early evaluation and optimization of radiotherapy in the near future, enabling the imaging of cell-cycle arrest and the associated suppression of cell proliferation *in vivo*.

Disclosure of Potential Conflicts of Interest

No potential conflicts of interest were disclosed.

Authors' Contributions

Conception and design: S. Saito, S. Hasegawa, I. Aoki
Development of methodology: S. Saito, I. Aoki
Acquisition of data (provided animals, acquired and managed patients, provided facilities, etc.): S. Saito, S. Hasegawa, A. Sekita
Analysis and interpretation of data (e.g., statistical analysis, biostatistics, computational analysis): S. Saito, S. Hasegawa, A. Sekita, I. Aoki

Published OnlineFirst May 21, 2013; DOI: 10.1158/0008-5472.CAN-12-3837

Writing, review, and/or revision of the manuscript: S. Saito, S. Hasegawa, R. Bakalova, T. Furukawa, T. Saga, I. Aoki
Administrative, technical, or material support (i.e., reporting or organizing data, constructing databases): S. Saito, A. Sekita
Study supervision: S. Saito, R. Bakalova, K. Murase, T. Saga, I. Aoki

Acknowledgments

The authors thank Sayaka Shibata, Takeo Shimomura, and Jeff Kershaw (National Institute of Radiological Sciences, Japan) for technical assistance and discussions. The authors also thank Takeshi Maeda, Hiroyuki Takano, and the FACS support team of the National Institute of Radiological Sciences for their technical assistance during the experiments using flow cytometry.

Grant Support

This work was partly supported by Grants-in-Aid for Scientific Research (Kakenhi) of the Japan Society for the Promotion of Science (JSPS) and the Funding Program for World-Leading Innovative R&D on Science and Technology (FIRST Program).

The costs of publication of this article were defrayed in part by the payment of page charges. This article must therefore be hereby marked *advertisement* in accordance with 18 U.S.C. Section 1734 solely to indicate this fact.

Received October 10, 2012; revised February 19, 2013; accepted March 6, 2013; published OnlineFirst May 21, 2013.

References

1. Greco C, Wolden S. Current status of radiotherapy with proton and light ion beams. Cancer 2007;109:1227–38.
2. Jones B. The potential clinical advantages of charged particle radiotherapy using protons or light ions. Clin Oncol (R Coll Radiol) 2008; 20:555–63.
3. Miyamoto T [Heavy ion therapy for non–small cell lung cancer–new, radical radiotherapy for advanced-age patients as an alternative to surgery]. Gan To Kagaku Ryoho 2003;30:209–14.
4. Kanematsu N, Asakura H, Kohno R, Takahashi O. Tumour shapes and fully automated range compensation for heavy charged particle radiotherapy. Phys Med Biol 2004;49:N1–5.
5. Wilson GD, Martindale CA, Soranson JA, Bourhis J, Carl UM, McNally NJ. Radiation-induced cell cycle delay measured in two mouse tumors *in vivo* using bromodeoxyuridine. Radiat Res 1994; 137:177–85.
6. Di Leonardo A, Linke SP, Clarkin K, Wahl GM. DNA damage triggers a prolonged p53-dependent G1 arrest and long-term induction of Cip1 in normal human fibroblasts. Genes Dev 1994;8:2540–51.
7. Suzuki K, Mori I, Nakayama Y, Miyakoda M, Kodama S, Watanabe M. Radiation-induced senescence-like growth arrest requires TP53 function but not telomere shortening. Radiat Res 2001;155:248–53.
8. DeSimone JN, Dolezalova H, Redpath JL, Stanbridge EJ. Prolonged cell cycle arrest in irradiated human diploid skin fibroblasts: the role of nutrient deprivation. Radiat Res 2000;153:131–43.
9. Dimri GP, Lee X, Basile G, Acosta M, Scott G, Roskelley C, et al. A biomarker that identifies senescent human cells in culture and in aging skin *in vivo*. Proc Natl Acad Sci U S A 1995;92:9363–7.
10. Koretsky AP, Silva AC. Manganese-enhanced magnetic resonance imaging (MEMRI). NMR Biomed 2004;17:527–31.
11. Silva AC, Lee JH, Aoki I, Koretsky AP. Manganese-enhanced magnetic resonance imaging (MEMRI): methodological and practical considerations. NMR Biomed 2004;17:532–43.
12. Aoki I, Naruse S, Tanaka C. Manganese-enhanced magnetic resonance imaging (MEMRI) of brain activity and applications to early detection of brain ischemia. NMR Biomed 2004;17:569–80.
13. Aschner M. Manganese homeostasis in the CNS. Environ Res 1999;80:105–9.
14. Itoh K, Sakata M, Watanabe M, Aikawa Y, Fujii H. The entry of manganese ions into the brain is accelerated by the activation of *N*-methyl-D-aspartate receptors. Neuroscience 2008;154:732–40.
15. Pautler RG, Koretsky AP. Tracing odor-induced activation in the olfactory bulbs of mice using manganese-enhanced magnetic resonance imaging. Neuroimage 2002;16:441–8.
16. Seshadri M, Hoy A. Manganese-enhanced MRI of salivary glands and head and neck tumors in living subjects. Magn Reson Med 2010; 64:902–6.
17. Braun RD, Gradianu M, Vistisen KS, Roberts RL, Berkowitz BA. Manganese-enhanced MRI of human choroidal melanoma xenografts. Invest Ophthalmol Vis Sci 2007;48:963–7.
18. Braun RD, Bissig D, North R, Vistisen KS, Berkowitz BA. Human tumor cell proliferation evaluated using manganese-enhanced MRI. PLoS ONE 2012;7:e30572.
19. Hu TC, Bao W, Lenhard SC, Schaeffer TR, Yue TL, Willette RN, et al. Simultaneous assessment of left-ventricular infarction size, function and tissue viability in a murine model of myocardial infarction by cardiac manganese-enhanced magnetic resonance imaging (MEMRI). NMR Biomed 2004;17:620–6.
20. Waghorn B, Schumacher A, Liu J, Jacobs S, Baba A, Matsuda T, et al. Indirectly probing Ca(2+) handling alterations following myocardial infarction in a murine model using T(1)-mapping manganese-enhanced magnetic resonance imaging. Magn Reson Med 2011;65: 239–49.
21. Inanami O, Iizuka D, Iwahara A, Yamamori T, Kon Y, Asanuma T, et al. A novel anticancer ribonucleoside, 1-(3-C-ethynyl-beta-D-ribo-pentofuranosyl)cytosine, enhances radiation-induced cell death in tumor cells. Radiat Res 2004;162:635–45.
22. Barrett PQ, Kojima I, Kojima K, Zawalich K, Isales CM, Rasmussen H. Short term memory in the calcium messenger system. Evidence for a sustained activation of protein kinase C in adrenal glomerulosa cells. Biochem J 1986;238:905–12.
23. Capiod T, Shuba Y, Skryma R, Prevarskaya N. Calcium signalling and cancer cell growth. Subcell Biochem 2007;45:405–27.
24. Dawitz J, Kroon T, Hjorth JJ, Meredith RM. Functional calcium imaging in developing cortical networks. J Vis Exp 2011;56:e3550.
25. Mihai R, Stevens J, McKinney C, Ibrahim NB. Expression of the calcium receptor in human breast cancer–a potential new marker predicting the risk of bone metastases. Eur J Surg Oncol 2006;32:511–5.
26. de Sousa PL, de Souza SL, Silva AC, de Souza RE, de Castro RM. Manganese-enhanced magnetic resonance imaging (MEMRI) of rat brain after systemic administration of $MnCl_2$: changes in T1 relaxation times during postnatal development. J Magn Reson Imaging 2007; 25:32–8.
27. Kawai Y, Aoki I, Umeda M, Higuchi T, Kershaw J, Higuchi M, et al. *In vivo* visualization of reactive gliosis using manganese-enhanced magnetic resonance imaging. Neuroimage 2010;49:3122–31.
28. Pautler RG. *In vivo*, trans-synaptic tract-tracing utilizing manganese-enhanced magnetic resonance imaging (MEMRI). NMR Biomed 2004; 17:595–601.
29. Hu TC, Christian TF, Aletras AH, Taylor JL, Koretsky AP, Arai AE. Manganese enhanced magnetic resonance imaging of normal and ischemic canine heart. Magn Reson Med 2005;54:196–200.
30. Anderson M. Mn ions pass through calcium channels. A possible explanation. J Gen Physiol 1983;81:805–27.
31. Narita K, Kawasaki F, Kita H. Mn and Mg influxes through Ca channels of motor nerve terminals are prevented by verapamil in frogs. Brain Res 1990;510:289–95.
32. Lin YJ, Koretsky AP. Manganese ion enhances T1-weighted MRI during brain activation: an approach to direct imaging of brain function. Magn Reson Med 1997;38:378–88.
33. Kita H, Narita K, Van der Kloot W. Tetanic stimulation increases the frequency of miniature end-plate potentials at the frog neuromuscular junction in Mn^{2+}-, CO^{2+}-, and Ni^{2+}-saline solutions. Brain Res 1981;205:111–21.
34. Baio G, Fabbi M, Emionite L, Cilli M, Salvi S, Ghedin P, et al. *In vivo* imaging of human breast cancer mouse model with high level expression of calcium sensing receptor at 3T. Eur Radiol 2012;22:551–8.
35. Wideroe M, Olsen O, Pedersen TB, Goa PE, Kavelaars A, Heijnen C, et al. Manganese-enhanced magnetic resonance imaging of hypoxic–ischemic brain injury in the neonatal rat. Neuroimage 2009; 45:880–90.

Published OnlineFirst May 21, 2013; DOI: 10.1158/0008-5472.CAN-12-3837

36. Hasegawa S, Koshikawa-Yano M, Saito S, Morokoshi Y, Furukawa T, Aoki I, *et al. Molecular imaging of mesothelioma by detection of manganese-superoxide dismutase activity using manganese-enhanced magnetic resonance imaging.* Int J Cancer 2011;128:2138–46.
37. Hasegawa S, Saito S, Koshikawa-Yano M, Furukawa T, Aoki I, Saga T. Tumor enhancement effect of overexpressed manganese-superoxide dismutase in manganese-enhanced MR imaging. Magn Reson Med Sci 2011;10:155–8.
38. Wahl M, Gruenstein E. Intracellular free Ca2+ in the cell cycle in human fibroblasts: transitions between G1 and G0 and progression into S phase. Mol Biol Cell 1993;4:293–302.
39. Lu KP, Osmani SA, Osmani AH, Means AR. Essential roles for calcium and calmodulin in G2/M progression in *Aspergillus nidulans*. J Cell Biol 1993;121:621–30.
40. Kishimoto T, Okumura E. *In vivo regulation of the entry into M-phase:* initial activation and nuclear translocation of cyclin B/Cdc2. Prog Cell Cycle Res 1997;3:241–9.
41. Crompton NE, Hain J, Jaussi R, Burkart W. Staurosporine- and *radiation-induced G2-phase cell cycle blocks are equally released by* caffeine. Radiat Res 1993;135:372–9.
42. Lindsay HD, Whitaker MJ, Ford CC. Calcium requirements during mitotic cdc2 kinase activation and cyclin degradation in *Xenopus* egg extracts. J Cell Sci 1995;108 (Pt 11):3557–68.
43. Alenzi FQ. Links between apoptosis, proliferation and the cell cycle. Br J Biomed Scie 2004;61:99–102.
44. Cuzick J, Dowsett M, Pineda S, Wale C, Salter J, Quinn E, et al. Prognostic value of a combined estrogen receptor, progesterone receptor, Ki-67, and human epidermal growth factor receptor 2 immunohistochemical score and comparison with the genomic health recurrence score in early breast cancer. J Clin Oncol 2011; 29:4273–8.
45. *Liu J, Li Z, Cui J, Xu G, Cui G. Cellular changes in the tumor micro-*environment of human esophageal squamous cell carcinomas. Tumour Biol 2011;33:495–505.

Journal of Controlled Release 169 (2013) 220–227

Contents lists available at SciVerse ScienceDirect

Journal of Controlled Release

journal homepage: www.elsevier.com/locate/jconrel

SPIO-PICsome: Development of a highly sensitive and stealth-capable MRI nano-agent for tumor detection using SPIO-loaded unilamellar polyion complex vesicles (PICsomes)

Daisuke Kokuryo [a,1], Yasutaka Anraku [b,1], Akihiro Kishimura [b,*], Sayaka Tanaka [c], Mitsunobu R. Kano [c], Jeff Kershaw [a], Nobuhiro Nishiyama [d], Tsuneo Saga [a], Ichio Aoki [a,**], Kazunori Kataoka [b,e,***]

[a] Molecular Imaging Center, National Institute of Radiological Sciences, Chiba-city 263-8555, Japan
[b] Department of Materials Engineering, Graduate School of Engineering, The University of Tokyo, Tokyo 113-8656, Japan
[c] Department of Pharmaceutical Biomedicine, Graduate School of Medicine, Dentistry and Pharmaceutical Sciences, Okayama University, Okayama 700-8530, Japan
[d] Polymer Chemistry Division, Chemical Resources Laboratory, Tokyo Institute of Technology, Yokohama 226-8503, Japan
[e] Center for Disease Biology and Integrative Medicine, Graduate School of Medicine, The University of Tokyo, Tokyo 113-8656, Japan

ARTICLE INFO

Article history:
Received 1 December 2012
Accepted 22 March 2013
Available online 29 March 2013

Keywords:
Polyion complex vesicles (PICsomes)
Magnetic resonance imaging (MRI)
Superparamagnetic iron oxide nanoparticles (SPIOs)
Drug delivery system
Tumor diagnosis

ABSTRACT

Size controllable polyion complex vesicles (PICsomes), composed of biocompatible poly(ethylene glycol) (PEG) and poly(amino acid)s, have an extremely prolonged lifetime in the bloodstream that enables them to accumulate effectively in tumors via the enhanced permeability and retention (EPR) effect. The purpose of this study was to use PICsomes to synthesize a highly sensitive MRI contrast agent for more precise tumor detection. We synthesized SPIO-Cy5-PICsomes (superparamagnetic iron oxide nanoparticle-loaded Cy5-cross-linked Nano-PICsomes) and characterized them using dynamic light scattering and transmission electron microscopy *in vitro* and evaluated their ability to detect subcutaneously grafted tumors *in vivo* with MRI. The transverse relaxivity (r_2) of the SPIO-Cy5-PICsomes ($r_2 = 663 \pm 28\ mM^{-1}\ s^{-1}$) was 2.54 times higher than that of bare clinically-used SPIO. In *in vivo* MRI experiments on mice subcutaneously grafted with colon-26 tumor cells, the tumor signal was significantly altered at 3 h after SPIO-Cy5-PICsome administration and persisted for at least 24 h. Small and early-stage *in vivo* tumors (3 days after grafting, approximately 4 mm^3) were also clearly detected with MRI. SPIO-loaded PICsomes are sensitive MRI contrast agents that can act as a powerful nanocarrier to detect small tumors for early diagnosis.

1. Introduction

The detection of early-stage tumors, especially during the early phase of metastasis, is important for improving treatment efficacy and prolonging patient survival. Non-invasive *in vivo* imaging, such as with magnetic resonance imaging (MRI) and positron emission tomography (PET), is critical for detecting disease in its early phase, and for that reason many biomedical applications utilize these techniques [1]. One advantage that MRI has over PET is that it can image at higher spatial resolutions [2]. However, low sensitivity to exogenous molecular probes (contrast agents) is a major limitation of MRI in comparison with PET. It is therefore necessary to engineer the properties of the probe to optimize its sensitivity for MRI.

Carboxyl dextran-coated superparamagnetic iron oxide (SPIO) nanoparticles are good 'negative' contrast agents for improving MRI contrast and have been used for clinical diagnosis and in pre-clinical cancer studies [3,4]. In clinical research, commercial SPIO nanoparticles, such as ferucarbotran (Resovist®) or ferumoxides (Feridex®), have been applied to detect metastatic tumors in the liver [5–8]. Unfortunately, carboxyl dextran-coated SPIO by itself does not have the ability to target tumors because Kupffer cells in healthy regions of the liver capture the SPIOs, with the result that the majority of the effect on the MRI signal occurs in the liver rather than in the tumor regions [6,7]. Therefore, to target tumors directly with SPIO nanoparticles, it is necessary to add a 'stealth' property in order to avoid recognition by the reticuloendothelial system (RES) and increase the lifetime of SPIOs in the bloodstream [3,9].

One strategy to achieve this stealth capability is to encapsulate the SPIOs in other nanoparticles that have prolonged lifetimes in the bloodstream and can passively accumulate in tumors due to the enhanced permeability and retention (EPR) effect [10]. Biocompatible poly(ethylene glycol) (PEG)-conjugated SPIOs or SPIO-loaded

* Correspondence to: A. Kishimura, 7-3-1 Hongo, Bunkyo-ku, Tokyo 113-8656, Japan. Tel.: +81 3 5841 7109; fax: +81 3 5841 7139.
** Correspondence to: I. Aoki, 4-9-1 Anagawa, Inage-ku, Chiba-city 263-8555, Japan. Tel.: +81 43 206 3272; fax: +81 43 206 3276.
*** Correspondence to: K. Kataoka, 7-3-1 Hongo, Bunkyo-ku, Tokyo 113-8656, Japan. Tel.: +81 3 5841 7138; fax: +81 3 5841 7139.
E-mail addresses: kishimura@bmw.t.u-tokyo.ac.jp (A. Kishimura), aoki@nirs.go.jp (I. Aoki), kataoka@bmw.t.u-tokyo.ac.jp (K. Kataoka).
[1] These two authors contributed equally.

0168-3659/$ – see front matter © 2013 Elsevier B.V. All rights reserved.
http://dx.doi.org/10.1016/j.jconrel.2013.03.016

nano-carriers have previously been employed to target tumors with SPIOs, with the targeting strategies falling into the following three groups: 1) PEG-conjugated SPIOs [11–15], 2) Ultra-small SPIO (USPIO)-loaded PEGylated micelles [16–20], and 3) SPIO-loaded PEGylated nano-vesicles [21–23]. Although the use of PEG-conjugated SPIOs is a simple strategy to prevent rapid clearance from the bloodstream, the direct conjugation of PEG to clinically-used SPIOs still has several drawbacks. First, stable and highly dense conjugation of PEG chains on the surface of SPIOs is technically difficult because the conjugation between PEG chains and carboxyl dextran is not stable, especially in the bloodstream. Accordingly, some additional surface modifications are required to achieve stable conjugation between PEG and SPIO nanoparticles [24]. Another drawback is that PEG-conjugated SPIOs have limited internal space, making it difficult to load them with drug levels sufficient for future therapeutic applications.

USPIO-loaded polymeric micelles have a moderately long blood half-life, and the high density of USPIOs that can be loaded into the micelle core noticeably alters the signal in comparison to dispersed USPIOs. It is unfortunate that when loaded with larger diameter SPIOs the micelles have an inadequate lifetime in the physiological environment of the bloodstream. On the other hand, SPIO-loaded PEGylated nano-vesicles, such as stealth liposomes, are designed to have longer circulation in the bloodstream and can be loaded with multiple iron-oxide particles, even if the particles are coated with carboxyl dextran [21–23]. In general, iron-oxide particles of larger size (SPIO > USPIO) or at a higher concentration can induce a greater signal change in T_2-weighted MRI due to T_2 and T_2^* shortening [25,26]. Thus, SPIO-loaded nano-vesicles may significantly enhance the contrast while simultaneously maintaining a high level of clinical safety and an increased blood half-life [27–30].

Recognizing the advantages of PEGylated nano-vesicles, we have developed and optimized polyion complex (PIC) nano-vesicles, called PICsomes. The PICsomes are generated by mixing water-soluble and oppositely charged block copolymers composed of biocompatible PEG and poly(amino acid)s in an aqueous medium [31–34]. PICsomes are characterized by the facile encapsulation of bio-macromolecules, such as dextran and proteins, and long-term retention and protection of cargo, regardless of external influences [32]. More recently, we have succeeded in preparing nano-sized PICsomes (Nano-PICsomes) with a unilamellar PIC membrane [33]. Unlike liposomal nano-carriers, the size of the Nano-PICsomes can be controlled with precision between 100 and 400 nm. After cross-linking the PIC layer via amide coupling of ion pairs, Nano-PICsomes remain in the blood circulation of mice for an extremely long time [34]. The blood lifetime of cross-linked Nano-PICsomes is comparable to that of typical long-lived liposomes and polymersomes [35]. Cross-linked Nano-PICsomes with diameters of approximately 100 nm also show excellent tumor accumulation due to the EPR effect [10]. However, the *in vivo* behavior of Nano-PICsomes containing payloads of contrast agents has not yet been evaluated.

Here, we report the first example of an MRI contrast agent using Nano-PICsomes, named 'SPIO-loaded Cy5-cross-linked Nano-PICsomes (SPIO-Cy5-PICsomes)', which enables targeted tumor imaging. SPIO-Cy5-PICsomes, which we designed and synthesized, are created from the combination of Nano-PICsomes and FDA-approved SPIO nanoparticles. The *in vitro* and *in vivo* performance of SPIO-Cy5-PICsomes was evaluated and characterized for a colon tumor, which is the third most common cancer in both men and women, in a subcutaneous transplanted mouse model. We also investigated the detection of small and early-phase tumors in a similar mouse model.

2. Materials and methods

2.1. Materials

1-ethyl-3-(3-dimethylaminopropyl) carbodiimide hydrochloride (EDC) was purchased from Wako Pure Chemical Industries (Osaka, Japan). A Cy5 mono-reactive dye pack and Sephacryl™ S-1000 gel were purchased from GE Healthcare (Tokyo, Japan). Block-aniomer, PEG-*b*-poly(α,β-aspartic acid) (PEG-PAsp, *Mn* of PEG = 2000, degree of polymerization (DP) of PAsp = 75) and homo-catiomer, poly([5-aminopentyl]-α,β-aspartamide) (Homo-P(Asp-AP), DP of P(Asp-AP) = 82) and Cy5-labeled PEG-PAsp (Cy5-PEG-PAsp) were prepared as previously reported [33]. Ferucarbotran (Resovist®) was purchased from Fujifilm RI Pharma (Tokyo, Japan).

2.2. Preparation and characterization of SPIO-Cy5-PICsomes

Solutions of Cy5-PEG-PAsp (2 mg/mL) and Homo-P(Asp-AP) (1 mg/mL) were prepared separately in 10 mM phosphate buffer (PB, pH 7.4, 0 mM NaCl). A ferucarbotran solution (Fe concentration = 2.9 mg/mL) was mixed with an equal volume of the Cy5-PEG-PAsp to prepare a Cy5-PEG-PAsp/SPIO solution (final concentrations: Cy5-PEG-PAsp, 1 mg/mL; and ferucarbotran, 1.5 mg/mL). Subsequently, the Cy5-PEG-PAsp/SPIO solution was mixed with the Homo-P(Asp-AP) solution with an equal unit ratio of $-COO^-$ and $-NH_3^+$ in the charged polymers and then vigorously stirred with a vortex mixer to prepare SPIO-Cy5-PICsomes. The SPIO-Cy5-PICsome solution was then added to the EDC solution (10 mg/mL, 10 eqv. per –COOH group in Cy5-PEG-PAsp). After 12 h, the mixed solution was purified using preparative gel permeation chromatography (GPC, column: Sephacryl™ S-1000, GE Healthcare UK, England). The size of the PICsomes was evaluated by dynamic light scattering (DLS) measurements at 25 °C using a Zetasizer Nano-ZS instrument (Malvern Instruments, Malvern, UK) equipped with a He-Ne ion laser (λ = 633 nm). The Fe content of the SPIO-Cy5-PICsomes was 16.1 ± 0.5 mM, as determined by inductively coupled plasma-mass spectroscopy (ICP-MS) performed with a 4500 ICP-MS instrument (Hewlett Packard, Palo Alto, CA, USA).

2.3. Transmission electron microscopy (TEM)

TEM was performed on a HITACHI H-7000 electron microscope operating at 75 kV. Copper grids of 400-mesh were coated with a thin film of formvar, followed by subsequent coating with carbon. Then, 1 μL of the sample solution was placed on the resulting grids and dried at room temperature. The samples were stained by the deposition of a drop of a 50% ethanol solution containing 2 wt.% uranyl acetate onto the surface of the sample-loaded grid and dried at room temperature.

2.4. R_2 and r_2 measurement in vitro

To measure the transverse relaxation rate (R_2), which is the reciprocal of the transverse relaxation time (T_2), of water protons (^1H) in the presence or absence of SPIO-Cy5-PICsomes, an *in vitro* MRI measurement was performed for SPIO-Cy5-PICsomes and bare ferucarbotran (n = 3). The SPIO-Cy5-PICsomes, diluted with phosphate-buffered saline, were prepared and loaded with the same Fe concentrations as control samples of SPIO nanoparticles, and then aliquoted into 0.2 mL PCR tubes. ICP-MS measurements were made to ensure that the Fe concentrations of the SPIO-Cy5-PICsomes and control samples were equal. MRI acquisitions were performed on a 7.0 Tesla, 40 cm bore magnet (Kobelco and Jastec, Kobe, Japan) interfaced to an Avance I system (Bruker-Biospin, Ettlingen, Germany) with a 35-mm diameter volume coil (Rapid Biomedical, Lymper, Germany). The sample temperature was maintained at 23 °C using a gradient-coil cooling system and air conditioners. Two-dimensional multi-spin-echo images were acquired with the following parameters: repetition time (TR)/echo time (TE) = 3000/10–100 ms in steps of 10 ms (10 echoes); field of view (FOV) = 48.0 × 48.0 mm^2; matrix = 256 × 256; resolution = 188 μm × 188 μm; number of slices = 1; slice thickness = 2.0 mm; slice direction = horizontal; and number of acquisitions (NEX) = 1. The scanning time was 12 min 48 s. After image

acquisition, the T_2 and R_2 were estimated using the MRVision image processing software (version 1.6.8, MR vision Co., MA, USA). The transverse relaxivity (r_2) was calculated with the equation; $r_2 = (R_{2obs} - R_{2d})/[Fe]$ (R_{2obs}: R_2 of the sample, R_{2d}: R_2 of the aqueous solution, [Fe]: Fe concentration measured by ICP-MS). Delta R_2 (ΔR_2) maps were calculated as ΔR_2 = (R_2 of the tumor after SPIO-Cy5-PICsome administration) − (R_2 of the tumor before administration).

2.5. Animal and cell line preparation

Overall, nineteen female BALB/c nude mice (Japan SLC, Shizuoka, Japan) were used for all *in vivo* studies. Ten animals were used to evaluate the accumulation of SPIO-Cy5-PICsomes in tumor: five were administered SPIO-Cy5-PICsomes and five were used for the ferucarbotran control. Another three animals were used for small tumor detection. The remaining six animals were used to test the toxicity of the SPIO-Cy5-PICsomes: three were administered SPIO-Cy5-PICsomes and three were used for the ferucarbotran control. The mice were maintained in accordance with the guidelines of the National Institute of Radiological Sciences (NIRS), and all experiments were reviewed and approved by the institute's committee for care and use of laboratory animals.

Colon -26 murine cancer cells were obtained from the RIKEN BioResource Center (Tukuba, Japan). The cells were maintained in Dulbecco's modified Eagle's medium (D5796, Sigma-Aldrich, St Louis, Mo, USA) supplemented with 10% fetal bovine serum, and incubated in a humidified atmosphere of 5% CO_2 in air at 37 °C. After suspension in phosphate-buffered saline, the cells were subcutaneously grafted (1.0×10^6 cells/50 μl) into the left flank of the mice. To measure the initial tumor volume before SPIO-Cy5-PICsome administration, T_2-weighted fast spin-echo images were acquired using a rapid acquisition with relaxation enhancement (RARE) sequence. The imaging parameters were as follows: TR/TE = 2000/40 ms; FOV = 38.4 × 38.4 mm^2; matrix = 256 × 256; resolution = 150 μm × 150 μm; number of slices = 36; slice thickness = 1.0 mm; slice direction = transaxial; RARE factor = 8; and NEX = 2.

2.6. Toxicity test

To evaluate the toxicity of the SPIO-Cy5-PICsomes to mice, the body weight of six BALB/c nude mice (age over 6 weeks-old) was periodically monitored before and after the administration of SPIO-Cy5-PICsomes (n = 3, initial body weight = 17.4 ± 1.2 g) or ferucarbotran (n = 3, initial body weight = 17.9 ± 1.4 g). The SPIO-Cy5-PICsomes or ferucarbotran contained 0.45 mg/kg Fe, which is the dose of ferucarbotran used in the clinic.

2.7. Evaluation of SPIO-Cy5-PICsome accumulation in tumor

To evaluate the *in vivo* tumor accumulation of SPIO-Cy5-PICsomes, 2D multi spin-echo T_2-weighted images were acquired before and after the administration of the SPIO-Cy5-PICsomes. T_2 and R_2 maps were calculated with non-linear least squares fitting to the multi-echo images. The tumors were allowed to grow for 7 to 9 days after the tumor cell transplantation. SPIO-Cy5-PICsomes were intravenously administered to five mice (body weight = 17.9 ± 1.0 g, tumor volume = 107 ± 26 mm^3) in the MRI scanner. The SPIO-Cy5-PICsomes contained 0.45 mg/kg Fe, which is the same as a clinical dose of ferucarbotran. For long-term observation of SPIO-Cy5-PICsome dynamics in tumors, R_2 maps were calculated from multi-spin-echo T_2-weighted images acquired prior to and at 1, 3, 6 and 24 h after administration. After MRI acquisition, *in vivo* fluorescence images were taken using a Maestro EX 2D fluorescence imaging system (PerkinElmer, MA, USA) to confirm the accumulation of SPIO-Cy5-PICsomes in the tumors. The mice were awakened and returned to their cages after all imaging was completed. As a control study, ferucarbotran (Resovist®, 0.45 mg/kg Fe) was injected via the tail vein to a further five mice (body weight = 19.0 ± 1.8 g, tumor volume = 92 ± 40 mm^3).

During the *in vivo* MRI experiments, the rectal temperatures of the mice were monitored using an optical fiber thermometer (FOT-M, FISO Technology, Quebec, Canada) and maintained at approximately 36.5 ± 0.5 °C by warm air provided by a homemade automatic heating system based on an electric temperature controller (E5CN, Omron, Kyoto, Japan). The mice were anesthetized with 1.5–2.0% isoflurane (Escain, Mylan, Tokyo, Japan) gas and a 1:2 O_2:room-air mixture. T_2-weighted images were acquired using a multi-spin-echo sequence with parameters as follows: TR/TE = 3000/10–100 ms in steps of 10 ms (10 echoes); FOV = 38.4 × 19.2 mm^2; matrix = 256 × 128; resolution = 150 μm × 150 μm; number of slices = 9; slice thickness = 1.0 mm; slice gap = 0.5 mm; slice direction = transaxial; and NEX = 1. The scanning time was 6 min 24 s. After image acquisition, the T_2 maps were estimated using MRVision.

In vivo fluorescence images of the mice that received the SPIO-Cy5-PICsomes were acquired using a fluorescent imager (Maestro EX) with the following parameters: excitation filter = 576–621 nm; emission filter = 635 nm longpass; acquisition setting = 630–800 nm in 10 nm steps; acquisition time = 100 ms; and FOV = 12.0 × 12.0 cm^2. After acquisition, unmixed fluorescence information was extracted from the fluorescence spectrum using the Maestro software package (PerkinElmer).

After all imaging was completed for an animal, the grafted tumors were excised and immersed in formalin for histological analysis. The formalin-fixed samples were then paraffinized and thin-sectioned for either hematoxylin and eosin (HE) staining and observation with light microscopy (Keyence, Osaka, Japan), or the Cy5 dye in the accumulated PICsomes was directly observed with a confocal laser scanning microscope (LSM510 META, Carl Zeiss, Oberkochen, Germany).

2.8. Small and early-stage tumor detection

To investigate the possibility of detecting small and early-stage tumors with SPIO-Cy5-PICsomes, we performed *in vivo* MR imaging of three mice 3 days after tumor transplantation. MRI was performed prior to and 24 h after SPIO-Cy5-PICsome administration. The tumor volumes were approximately 4 mm^3 when measured before SPIO-Cy5-PICsome administration.

The MR images were acquired using a 7.0 Tesla, 20 cm bore magnet (Bioscan, Bruker-Biospin) interfaced to an Avance III system with a 2-ch high-sensitivity RF coil (CryoProbe™, Bruker-Biospin). The T_2-weighted images were acquired using a spin-echo sequence with the following parameters: TR/TE = 3000/30 ms; FOV = 25.6 × 12.8 or 19.2 mm^2; matrix = 256 × 128 or 192; resolution = 100 μm × 100 μm; number of slices = 9; slice thickness = 750 μm; slice gap = 250 μm; slice direction = transaxial; and NEX = 2. After MRI acquisition, fluorescence images were also acquired using the same parameters as described in the previous sections.

2.9. Statistical analysis

Alterations to R_2 for the SPIO-Cy5-PICsomes and bare SPIOs were statistically evaluated using a two-way ANOVA with the Bonferroni correction (Prism, Ver. 5, GraphPad Software, CA, USA). Changes to the body weight due to SPIO-Cy5-PICsomes and bare SPIOs were also statistically evaluated with the same test. A significance level of 0.05 was used.

3. Results and discussion

3.1. Chemical characterization of the SPIO-Cy5-PICsomes

The method used to prepare the PICsome nano-carrier was similar to that previously reported for macromolecule-loaded Nano-PICsomes

(Fig. 1) [33,34]. Fig. 2A presents a TEM image of ferucarbotran alone, the size of which is consistent with reported values [36,37]. Successful loading of ferucarbotran, seen as small black dots of approximately 30 nm in diameter, into the PICsome was confirmed in Fig. 2B. In this unstained TEM image, the ferucarbotran particles can be seen to overlap dark gray shadows (diameter approximately 100 nm), that correspond to the PICsomes. It is noteworthy that unencapsulated SPIOs were rarely observed in the SPIO-Cy5-PICsome samples, indicating an almost complete removal of the SPIOs by preparative GPC. Additionally, in the stained TEM images (Fig. S1), vesicular structures of a similar size to the shadows in Fig. 2B were found. The DLS result demonstrated a narrow size distribution for the SPIO-Cy5-PICsomes (Fig. 2C, average diameter = 102 nm, polydispersity index (PDI) = 0.056), that was consistent with the size of the black dots in the TEM images. The SPIO-Cy5-PICsomes were large enough to contain multiple SPIO nanoparticles, and multiple SPIOs encapsulated in a single Nano-PICsome were occasionally observed (Fig. 2B, white arrow).

3.2. In vitro R_2

The dependence of R_2 on iron concentration is shown in Fig. 2D and E. The R_2 of SPIO-Cy5-PICsomes was approximately twice as large as that of ferucarbotran (20 μM SPIO-Cy5-PICsomes: 15.86 ± 0.60 s^{-1}, ferucarbotran: 7.89 ± 0.67 s^{-1}). The r_2 of the SPIO-Cy5-PICsomes and ferucarbotran were 663 ± 28 mM^{-1} s^{-1} and 261 ± 30 mM^{-1} s^{-1}, respectively. There are two factors that may contribute to the larger r_2 of the SPIO-Cy5-PICsomes. The first is that, as shown in the TEM image (Fig. 2B), some of the SPIO-Cy5-PICsomes contain multiple SPIO nanoparticles. Having two or more SPIO nanoparticles in close proximity will perturb the shape of the surrounding magnetic field gradient and potentially increase the observed r_2. This effect has been shown in previous reports when the r_2 of aggregated SPIO or USPIO nanoparticles were enhanced in comparison to those of dispersed SPIO or USPIO nanoparticles [20,36–38]. The second factor that may influence the r_2 of SPIO-Cy5-PICsomes is the vesicle wall. As the experiment on empty Cy5-PICsomes indicated (Fig. 2E), the materials that compose the membrane do not affect r_2 significantly in comparison to pure saline. However, the paths of molecules diffusing through the field gradient near the SPIOs are influenced by the PIC layer or PEG chains on the PIC layer, and this could affect the observed r_2 [39,40].

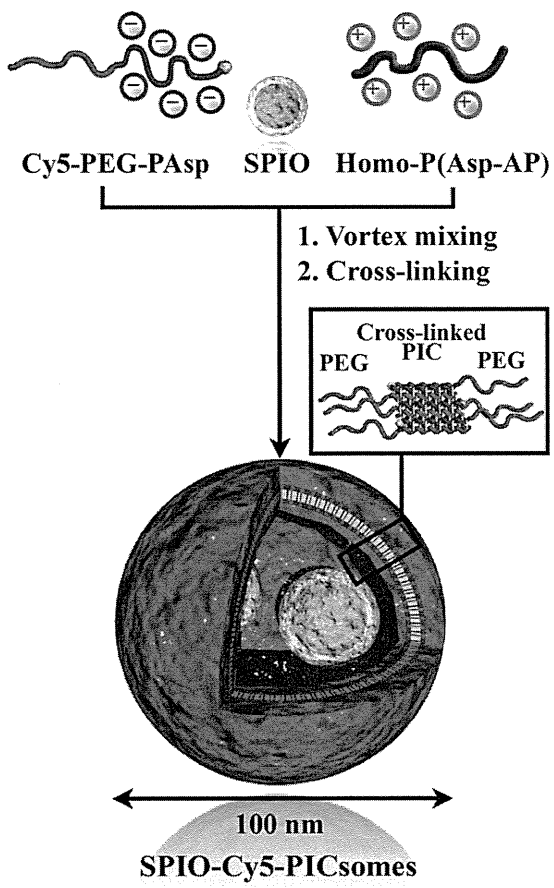

Fig. 1. Schematic representation of the SPIO-Cy5-PICsome preparation.

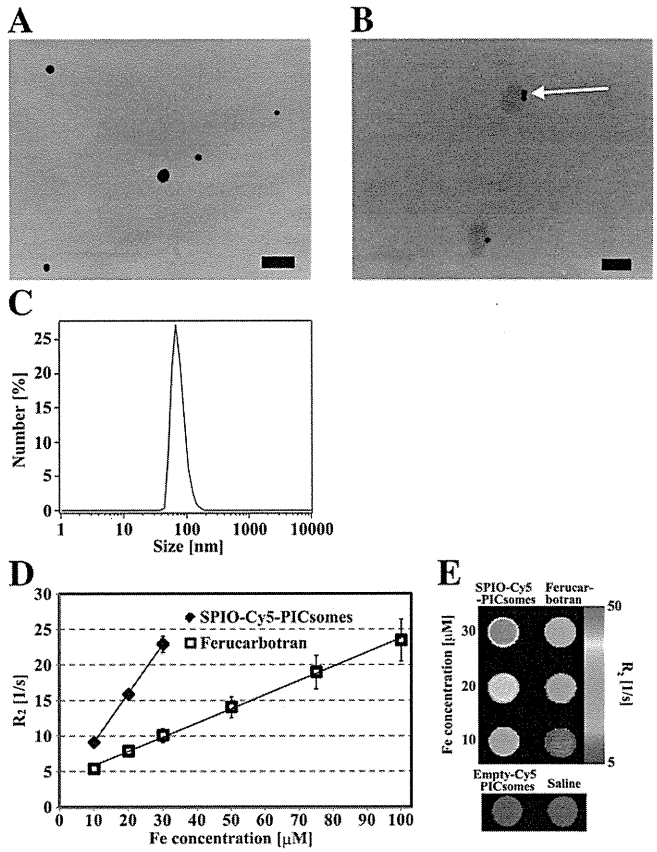

Fig. 2. Results of the *in vitro* TEM, DLS, and R_2 measurements. TEM images of (A) ferucarbotran and (B) SPIO-Cy5-PICsomes. The scale bar is 100 nm. (C) A typical size distribution for SPIO-Cy5-PICsomes determined by DLS. (D) Concentration dependence of R_2s. A straight line fit for the SPIO-Cy5-PICsomes gave $y = 0.69\ x + 2.16$ ($R^2 = 0.9998$), and for ferucarbotran $y = 0.20\ x + 3.86$ ($R^2 = 0.998$). (E) Representative R_2 mapping of SPIO-Cy5-PICsomes, ferucarbotran, empty Cy5-PICsomes and saline.

3.3. In vivo analysis of tumor accumulation using MR and fluorescence imaging

Typical T_2-weighted MRI and fluorescence images of tumor before and up to 24 h after SPIO-Cy5-PICsome administration are shown in Fig. 3. In the MR images, signal reductions were observed in the tumors at 3 h after the administration. In fact, as shown in Fig. S2, signal alteration in the tumor was detected at 2 h after the administration, and the area of the signal alteration expanded over the next 4 h. The signal alteration was maintained until at least 24 h after administration (Fig. 3). MRI signal alteration in the tumor was in agreement with the *in vivo* fluorescence imaging (Fig. 3). The results were further confirmed by histological analysis of the tumor, with the results shown in Fig. 4. HE staining of the thin-sectioned tumor revealed rich vascularization of the tumor area without showing significant degeneration like necrosis. As detected from the fluorescence of the Cy5 dye, the accumulation of the SPIO-Cy5-PICsomes was especially high in tumor areas that showed clear MRI signal reduction (Figs. 3 and 4).

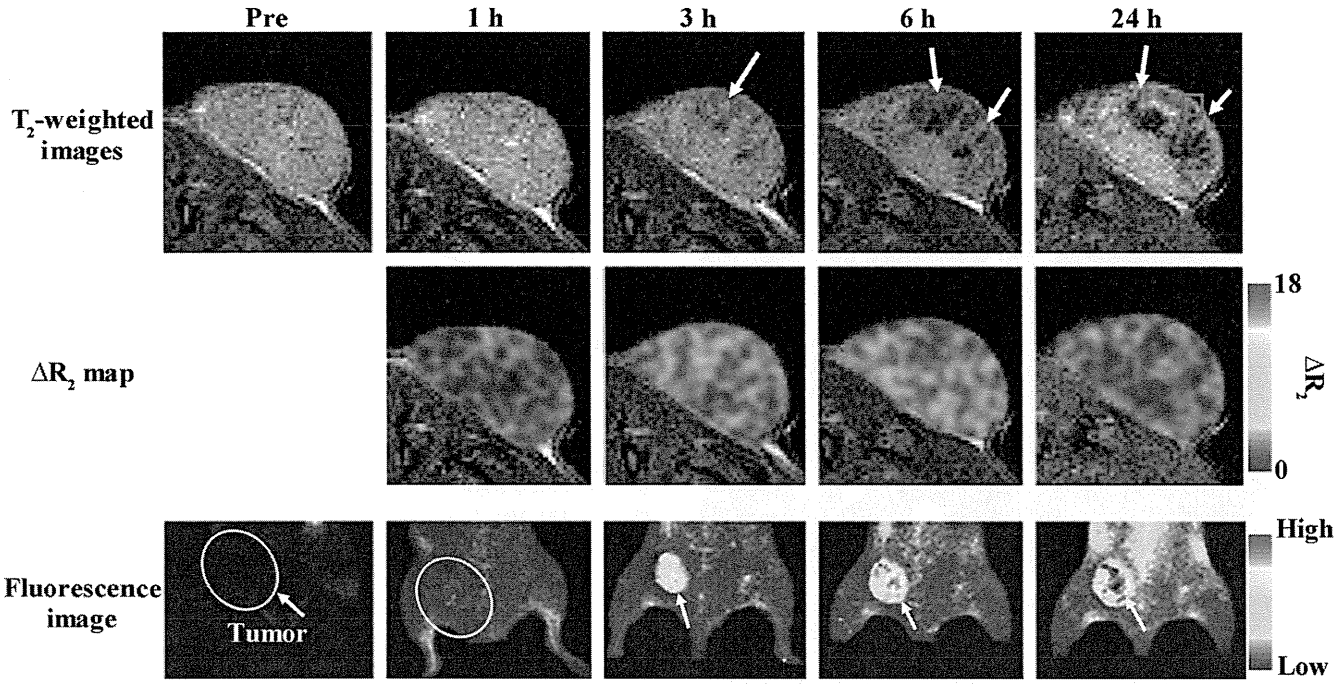

Fig. 3. Typical results of MRI and optical imaging of the *in vivo* tumor model. T_2-weighted MRIs (upper), ΔR_2 maps (middle), and fluorescence images (bottom) were obtained for up to 24 h after SPIO-Cy5-PICsome administration. The MRI signal in the tumor (arrows) was noticeably different 3 h after administration, and the area encompassing the signal change was clearly larger at 6 and 24 h after administration. For the fluorescence images, similar to the MRI the signal increased at 3 h after administration. The square in the 24 h T_2-weighted image corresponds to the area used for histological evaluation (see Fig. 4).

Fig. 5 shows how R_2 changed over the 24 h after SPIO-Cy5-PICsome or ferucarbotran administration. The R_2 of the tumor after SPIO-Cy5-PICsome administration gradually increased, and peaked with an increase of 30% at 6 h after administration in comparison to the values before administration (Fig. 5). At 24 h after administration, the R_2 remained at the same level as at 6 h. In contrast, the R_2 after ferucarbotran administration was significantly smaller than the values at 3, 6 and 24 h after SPIO-Cy5-PICsome administration (Fig. 5). These results are attributed to the facilitated EPR effect of SPIO-Cy5-PICsomes prolonging circulation in the bloodstream [34], and to the larger relaxivity (Fig. 2D). We also think that if our SPIO-Cy5-PICsomes are used, a tumor diagnosis might be made by comparing the MR images of 3 h and 24 h after administration.

Even though the pharmacokinetics of the SPIO-Cy5-PICsomes was not quantitatively investigated in this study, it is expected that they retain the same qualities as reported in our previous Cy5-PICsome study [34]. This is also supported by the low renal interaction of SPIO-Cy5-PICsomes, which was suggested by the negligible change in the MR signal intensity of kidney in the first 6 h after administration (Fig. S2), and sustained accumulation in the tumor between 3 and 24 h after administration (Figs. 3 and 5).

Changes in the body weight of the mice after SPIO-Cy5-PICsome or ferucarbotran administration are shown in Fig. S3. There were no significant changes during the week after SPIO-Cy5-PICsome administration. None of the animals exhibited other symptoms of systemic toxicity such as abnormal behavior or death after SPIO-Cy5-PICsome administration, even though a three times higher dose of SPIO-Cy5-PICsomes was administered (1.35 mg/kg Fe, Fig. S4).

As noted in the Introduction, SPIO-loaded PEGylated nano-vesicles have several advantages, including longer circulation in the bloodstream and the potential to carry multiple iron-oxide particles, that enables strong signal enhancement in tumor [21–23]. It should also be noted that SPIO or USPIO-loaded PEGylated liposomes have been applied for tumor detection and evaluation of tumor treatment with MRI [27–30]. It is our impression that PEGylated liposomes have characteristics that differ from Nano-PICsomes. The PEGylated liposomes have hydrophobic and non-permeable lipid membranes and can provide a platform for loading water-soluble drugs in a simple manner. However, the lipid membrane blocks communication between the inside and outside of the liposomes and it is technically difficult to conjugate with PEGs at a sufficiently high density. Therefore, liposomal formulations of this sort are not always favorable for *in vivo* sensing systems. On the other hand, Nano-PICsomes have a membrane that is permeable to low-molecular weight compounds, aids extremely prolonged circulation in the bloodstream, is a robust structure due to cross-linking, and forms a nano-particle of controllable diameter. These characteristics of Nano-PICsomes contribute to their potential to be carriers of sensor agents for probing the tissue environment *in vivo*; Nano-PICsomes are expected to accumulate selectively in tumors, working as highly sensitive MRI contrast agents.

3.4. Detection of small and early-stage tumor

Fig. 6 presents the T_2-weighted images of a small and early-stage tumor (3 days after grafting, approximately 4 mm^3) before (Fig. 6A and C) and 24 h after (Fig. 6B and D) SPIO-Cy5-PICsome administration. MRI signal alteration was detectable *in vivo*. The Cy5 fluorescence signal observed in the tumor region was in agreement with the MRI signal alteration (Fig. 6E). When the skin covering the tumor region was incised, it was observed that several vessels were connected to the small and early-stage tumor (Fig. 6F and G). These results indicate that SPIO-Cy5-PICsomes accumulate, presumably due to the EPR effect, even in a small tumor that only had 3 days of *in vivo* growth in immunodeficient mice. Hence, if the micro-metastases are connected to the vasculature it is likely that SPIO-Cy5-PICsomes will accumulate in the tumor and aid early stage detection.

The *in vivo* detection of small tumors has been performed using other tomographic imaging modalities such as PET and single photon

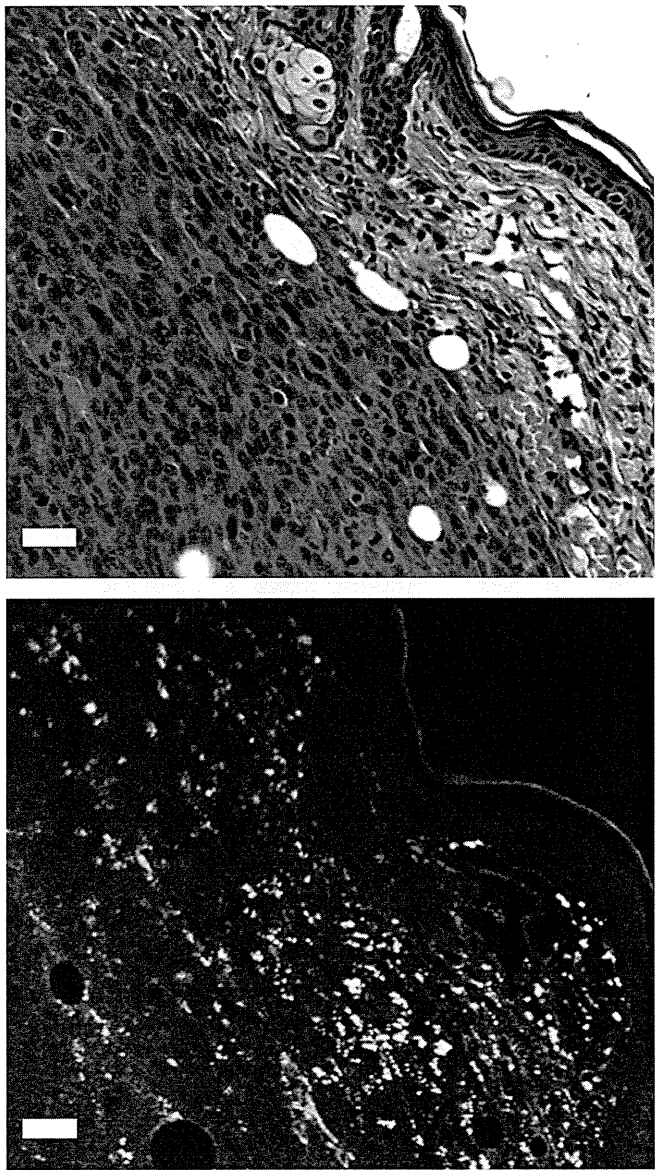

Fig. 4. Histological analysis of the tumor sample shown in Fig. 3. The sample was serially sectioned and underwent HE staining (top), and fluorescence imaging of the Cy5 dye (bottom). The white dots in the fluorescence image indicate SPIO-Cy5-PICsomes. Scale bar, 50 nm (observed with a ×20 objective lens).

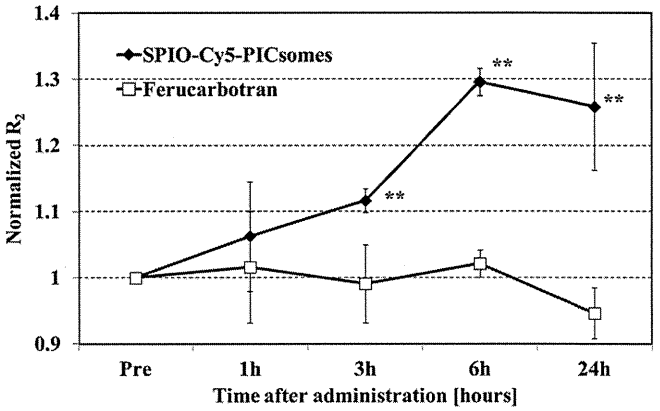

Fig. 5. Changes to the R_2 normalized by the value obtained before administration. The error bars denote the standard deviation. The closed diamonds correspond to tumors with SPIO-Cy5-PICsomes and the open squares to those with ferucarbotran. The level of significance was set at $p < 0.001$ (**) for a two-way ANOVA with Bonferroni correction.

emission computed tomography (SPECT) [41,42]. The minimum size of a detectable tumor was approximately 1 mm in diameter, which is smaller than the tumor size detected in our trial. Although highly sensitive PET and SPECT imaging might be able to detect smaller tumors deeply seated within the body without requiring invasive procedures, it is difficult to determine the precise position of the tumor because of the limited spatial resolution (approximately 2–3 mm) of those modalities. The high sensitivity of MRI to SPIO nanoparticles has been used to observe the migration of groups of cells [43–48], and in some cases track the paths of single cells [49]. Combined with the high spatial resolution ($100 \times 100\ \mu m^2$) of MRI, we therefore expect that SPIO-Cy5-PICsomes might be used to detect not only small tumors, but also their differential distribution due to variations in the micro-environment inside the tumor. Thus, SPIO-Cy5-PICsomes have the potential to provide novel diagnostic information for the clinic.

4. Conclusion

Ferucarbotran-loaded unilamellar polyion complex vesicles, SPIO-Cy5-PICsomes, were developed as highly sensitive MRI contrast agents that accumulate in tumors. The properties of the SPIO-Cy5-PICsomes were evaluated both *in vitro* and *in vivo*. The transverse relaxivity of the SPIO-Cy5-PICsomes was 2.54 times higher than that of dispersed ferucarbotran. In a subcutaneously grafted colon 26 cancer model, significant alterations in the tumor MRI signals were reliably detected at 3 h after SPIO-Cy5-PICsome administration and maintained for 24 h. A small, early-stage tumor was also visualized using both *in vivo* MRI and fluorescence imaging. SPIO-loaded PICsomes allow small metastatic tumors to be detected and this may contribute to earlier identification for treatment in the clinic. In addition, these results indicate that loaded cross-linked PICsomes display similar pharmacokinetic behavior to unloaded cross-linked PICsomes, suggesting that PICsomes can be a versatile platform for nano-medicines. Looking ahead, anti-cancer-drug-loaded SPIO-PICsomes have potential therapeutic applications.

Supplementary data to this article can be found online at http://dx.doi.org/10.1016/j.jconrel.2013.03.016.

Acknowledgments

The authors thank Sayaka Shibata and Aiko Sekita (NIRS) for helping with the animal experiments. This research was supported by the Japan Society for the Promotion of Science through the Funding Program for World-Leading Innovation R&D on Science and Technology (FIRST program). We are grateful to Dr. S. Fukuda at the University of Tokyo Hospital, and the staff of the Research Hub for Advanced Nano Characterization, The University of Tokyo, which is supported by MEXT of Japan, for their valuable support while performing the TEM measurements.

References

[1] M. Rudin, R. Weissleder, Molecular imaging in drug discovery and development, Nat. Rev. Drug Discov. 2 (2003) 123–131.
[2] T.F. Massoud, S.S. Gambhir, Molecular imaging in living subjects: seeing fundamental biological processes in a new light, Genes Dev. 17 (2003) 545–580.
[3] J.W. Bulte, D.L. Kraitchman, Iron oxide MR contrast agents for molecular and cellular imaging, NMR Biomed. 17 (2004) 484–499.
[4] Y.-X.J. Wang, Superparamagnetic iron oxide based MRI contrast agents: current status of clinical application, Quant. Imaging Med. Surg. 1 (2011) 35–40.
[5] J. Ward, K.S. Naik, J.A. Guthrie, D. Wilson, P.J. Robinson, Hepatic lesion detection: comparison of MR imaging after the administration of superparamagnetic iron oxide with dual-phase CT by using alternative-free response receiver operating characteristic analysis, Radiology 210 (1999) 459–466.

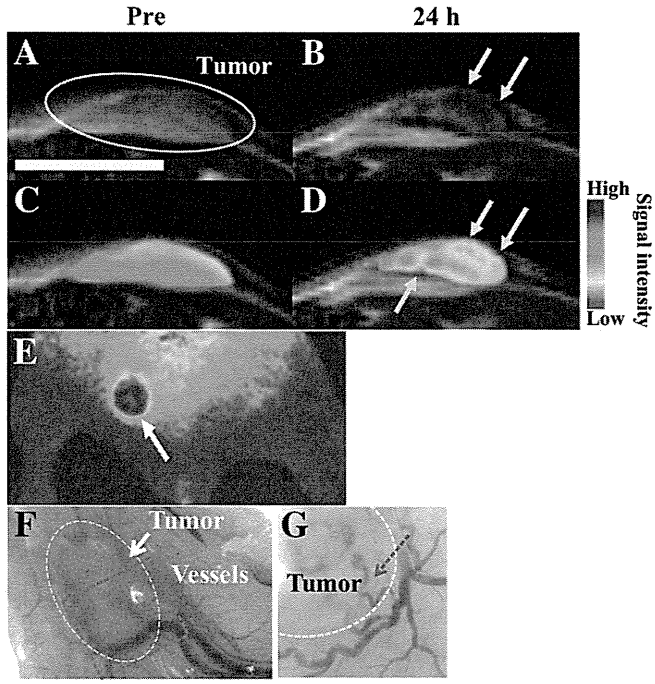

Fig. 6. Application of the SPIO-Cy5-PICsomes to small tumor detection. T_2-weighted MR images before (A, C) and at 24 h (B, D) after SPIO-Cy5-PICsome administration are shown. The tumor volume was approximately 4 mm^3. The scale bar has a length of 3 mm. The signal from the tumor (yellow arrows) at 24 h after the administration decreased from that before administration. In the fluorescence image (E) acquired 24 h after the administration, the signal from the tumor region (arrow) is higher than the signal from other regions. In the optical photo of the small tumor (F), several vessels can be seen connected to the tumor. It was confirmed that the vessels (blue dashed arrows) were connected to the tumor (outline highlighted by the white ellipse) in a higher magnification image (G) of the fixed tissue (blue square).

[6] J.H. Lim, D. Choi, S.K. Cho, S.H. Kim, W.J. Lee, H.K. Lim, C.K. Park, S.W. Paik, Y.I. Kim, Conspicuity of hepatocellular nodular lesions in cirrhotic livers at ferumoxides-enhanced MR imaging: importance of Kupffer cell number, Radiology 220 (2001) 669–676.
[7] A. Tanimoto, Y. Yuasa, H. Shinmoto, M. Jinzaki, Y. Imai, S. Okuda, S. Kuribayashi, Superparamagnetic iron oxide-mediated hepatic signal intensity change in patients with and without cirrhosis: pulse sequence effects and Kupffer cell function, Radiology 222 (2002) 661–666.
[8] Y. Lee, J.S. Lee, C.M. Kim, J.Y. Jeong, J.I. Choi, M.J. Kim, Area of paradoxical signal drop after the administration of superparamagnetic iron oxide on the T2-weighted image of a patient with lymphangitic metastasis of the liver, Magn. Reson. Imaging 26 (2008) 577–582.
[9] T. Schlorf, M. Meincke, E. Kossel, C.C. Gluer, O. Jansen, R. Mentlein, Biological properties of iron oxide nanoparticles for cellular and molecular magnetic resonance imaging, Int. J. Mol. Sci. 12 (2010) 12–23.
[10] Y. Matsumura, H. Maeda, A new concept for macromolecular therapeutics in cancer chemotherapy: mechanism of tumoritropic accumulation of proteins and the antitumor agent smancs, Cancer Res. 46 (1986) 6387–6392.
[11] Y. Tamaura, K. Takahashi, Y. Kodera, Y. Saito, Y. Inada, Chemical modification of lipase with ferromagnetic modifier—a ferromagnetic-modified lipase, Biotechnol. Lett. 8 (1986) 877–880.
[12] D.K. Kim, Y. Zhang, J. Kehr, T. Klason, B. Bjelke, M. Muhammed, Characterization and MRI study of surfactant-coated superparamagnetic nanoparticles administered into the rat brain, J. Magn. Magn. Mater. 225 (2001) 256–261.
[13] M. Kumagai, Y. Imai, T. Nakamura, Y. Yamasaki, M. Sekino, S. Ueno, K. Hanaoka, K. Kikuchi, T. Nagano, E. Kaneko, K. Shimokado, K. Kataoka, Iron hydroxide nanoparticles coated with poly(ethylene glycol)-poly(aspartic acid) block copolymer as novel magnetic resonance contrast agents for *in vivo* cancer imaging, Colloids Surf. B Biointerfaces 56 (2007) 174–181.
[14] H. Kojima, Y. Mukai, M. Yoshikawa, K. Kamei, T. Yoshikawa, M. Morita, T. Inubushi, T.A. Yamamoto, Y. Yoshioka, N. Okada, S. Seino, S. Nakagawa, Simple PEG conjugation of SPIO via an Au–S bond improves its tumor targeting potency as a novel MR tumor imaging agent, Bioconjug. Chem. 21 (2010) 1026–1031.
[15] G.B. Hong, J.X. Zhou, R.X. Yuan, Folate-targeted polymeric micelles loaded with ultrasmall superparamagnetic iron oxide: combined small size and high MRI sensitivity, Int. J. Nanomedicine 7 (2012) 2863–2872.
[16] N. Nasongkla, E. Bey, J. Ren, H. Ai, C. Khemtong, J.S. Guthi, S.F. Chin, A.D. Sherry, D.A. Boothman, J. Gao, Multifunctional polymeric micelles as cancer-targeted, MRI-ultrasensitive drug delivery systems, Nano Lett. 6 (2006) 2427–2430.
[17] H.J. Lee, K.S. Jang, S. Jang, J.W. Kim, H.M. Yang, Y.Y. Jeong, J.D. Kim, Poly(amino acid)s micelle-mediated assembly of magnetite nanoparticles for ultra-sensitive long-term MR imaging of tumors, Chem. Commun. (Camb.) 46 (2010) 3559–3561.
[18] J.S. Guthi, S.G. Yang, G. Huang, S. Li, C. Khemtong, C.W. Kessinger, M. Peyton, J.D. Minna, K.C. Brown, J. Gao, MRI-visible micellar nanomedicine for targeted drug delivery to lung cancer cells, Mol. Pharm. 7 (2010) 32–40.
[19] X. Yang, J.J. Grailer, I.J. Rowland, A. Javadi, S.A. Hurley, V.Z. Matson, D.A. Steeber, S. Gong, Multifunctional stable and pH-responsive polymer vesicles formed by heterofunctional triblock copolymer for targeted anticancer drug delivery and ultrasensitive MR imaging, ACS Nano 4 (2010) 6805–6817.
[20] W.I. Choi, J.Y. Kim, S.U. Heo, Y.Y. Jeong, Y.H. Kim, G. Tae, The effect of mechanical properties of iron oxide nanoparticle-loaded functional nano-carrier on tumor targeting and imaging, J. Control. Release 162 (2012) 267–275.
[21] J.X. Zhang, S.C. Dang, Y. Zhang, X. Sha, L.R. Zhang, C.S. Wei, M. Chen, D.L. Jiang, MRI shows clodronate-liposomes attenuating liver injury in rats with severe acute pancreatitis, Hepatobiliary Pancreat. Dis. Int. 9 (2010) 192–200.
[22] K. Katagiri, Y. Imai, K. Koumoto, T. Kaiden, K. Kono, S. Aoshima, Magnetoresponsive on-demand release of hybrid liposomes formed from Fe_3O_4 nanoparticles and thermosensitive block copolymers, Small 7 (2011) 1683–1689.
[23] T. Toyota, N. Ohguri, K. Maruyama, M. Fujinami, T. Saga, I. Aoki, Giant vesicles containing superparamagnetic iron oxide as biodegradable cell-tracking MRI probes, Anal. Chem. 84 (2012) 3952–3957.
[24] M. Kumagai, T.K. Sarma, H. Cabral, S. Kaida, M. Sekino, N. Herlambang, K. Osada, M.R. Kano, N. Nishiyama, K. Kataoka, Enhanced *in vivo* magnetic resonance imaging of tumors by PEGylated iron-oxide-gold core-shell nanoparticles with prolonged blood circulation properties, Macromol. Rapid Commun. 31 (2010) 1521–1528.
[25] E.M. Shapiro, S. Skrtic, A.P. Koretsky, Sizing it up: cellular MRI using micron-sized iron oxide particles, Magn. Reson. Med. 53 (2005) 329–338.
[26] R. Kuhlpeter, H. Dahnke, L. Matuszewski, T. Persigehl, A. von Wallbrunn, T. Allkemper, W.L. Heindel, T. Schaeffter, C. Bremer, R2 and R2* mapping for sensing cell-bound superparamagnetic nanoparticles: *in vitro* and murine *in vivo* testing, Radiology 245 (2007) 449–457.
[27] M.S. Martina, J.P. Fortin, C. Menager, O. Clement, G. Barratt, C. Grabielle-Madelmont, F. Gazeau, V. Cabuil, S. Lesieur, Generation of superparamagnetic liposomes revealed as highly efficient MRI contrast agents for *in vivo* imaging, J. Am. Chem. Soc. 127 (2005) 10676–10685.
[28] A. Wijaya, K. Hamad-Schifferli, High-density encapsulation of Fe_3O_4 nanoparticles in lipid vesicles, Langmuir 23 (2007) 9546–9550.
[29] M.E. Meyre, G. Raffard, J.M. Franconi, E. Duguet, O. Lambert, C. Faure, Production of magnetic multilamellar liposomes as highly T2-efficient MRI contrast agents, Nanomedicine 7 (2011) 18–21.
[30] G. Bealle, R. Di Corato, J. Kolosnjaj-Tabi, V. Dupuis, O. Clement, F. Gazeau, C. Wilhelm, C. Menager, Ultra magnetic liposomes for MR imaging, targeting, and hyperthermia, Langmuir 28 (2012) 11834–11842.
[31] A. Koide, A. Kishimura, K. Osada, W.D. Jang, Y. Yamasaki, K. Kataoka, Semipermeable polymer vesicle (PICsome) self-assembled in aqueous medium from a pair of

oppositely charged block copolymers: physiologically stable micro-/nanocontainers of water-soluble macromolecules, J. Am. Chem. Soc. 128 (2006) 5988–5989.
[32] A. Kishimura, A. Koide, K. Osada, Y. Yamasaki, K. Kataoka, Encapsulation of myoglobin in PEGylated polyion complex vesicles made from a pair of oppositely charged block ionomers: a physiologically available oxygen carrier, Angew. Chem. Int. Ed Engl. 46 (2007) 6085–6088.
[33] Y. Anraku, A. Kishimura, M. Oba, Y. Yamasaki, K. Kataoka, Spontaneous formation of nanosized unilamellar polyion complex vesicles with tunable size and properties, J. Am. Chem. Soc. 132 (2010) 1631–1636.
[34] Y. Anraku, A. Kishimura, A. Kobayashi, M. Oba, K. Kataoka, Size-controlled long-circulating PICsome as a ruler to measure critical cut-off disposition size into normal and tumor tissues, Chem. Commun. (Camb.) 47 (2011) 6054–6056.
[35] P.J. Photos, L. Bacakova, B. Discher, F.S. Bates, D.E. Discher, Polymer vesicles *in vivo*: correlations with PEG molecular weight, J. Control. Release 90 (2003) 323–334.
[36] J.F. Berret, K. Yokota, M. Morvan, R. Schweins, Polymer-nanoparticle complexes: from dilute solution to solid state, J. Phys. Chem. B 110 (2006) 19140–19146.
[37] J. Yang, C.H. Lee, H.J. Ko, J.S. Suh, H.G. Yoon, K. Lee, Y.M. Huh, S. Haam, Multifunctional magneto-polymeric nanohybrids for targeted detection and synergistic therapeutic effects on breast cancer, Angew. Chem. Int. Ed Engl. 46 (2007) 8836–8839.
[38] S.-M. Lai, J.-K. Hsiao, H.-P. Yu, C.-W. Lu, C.-C. Huang, M.-J. Shieh, P.-S. Lai, Polyethylene glycol-based biocompatible and highly stable superparamagnetic iron oxide nanoclusters for magnetic resonance imaging, J. Mater. Chem. 22 (2012) 15160–15167.
[39] Q.L. Vuong, P. Gillis, Y. Gossuin, Monte Carlo simulation and theory of proton NMR transverse relaxation induced by aggregation of magnetic particles used as MRI contrast agents, J. Magn. Reson. 212 (2011) 139–148.
[40] E. Poselt, H. Kloust, U. Tromsdorf, M. Janschel, C. Hahn, C. Masslo, H. Weller, Relaxivity optimization of a PEGylated iron-oxide-based negative magnetic resonance contrast agent for T(2)-weighted spin-echo imaging, ACS Nano 6 (2012) 1619–1624.
[41] M. Brom, L. Joosten, P. Laverman, W.J. Oyen, M. Behe, M. Gotthardt, O.C. Boerman, Preclinical evaluation of 68Ga-DOTA-minigastrin for the detection of cholecystokinin-2/gastrin receptor-positive tumors, Mol. Imaging 10 (2011) 144–152.
[42] V. Patil, K. Gada, R. Panwar, A. Varvarigou, S. Majewski, A. Weisenberger, C. Ferris, Y. Tekabe, B.A. Khaw, Imaging small human prostate cancer xenografts after pretargeting with bispecific bombesin-antibody complexes and targeting with high specific radioactivity labeled polymer-drug conjugates, Eur. J. Nucl. Med. Mol. Imaging 39 (2012) 824–839.
[43] J.W. Bulte, S. Zhang, P. van Gelderen, V. Herynek, E.K. Jordan, I.D. Duncan, J.A. Frank, Neurotransplantation of magnetically labeled oligodendrocyte progenitors: magnetic resonance tracking of cell migration and myelination, Proc. Natl. Acad. Sci. U. S. A. 96 (1999) 15256–15261.
[44] M. Modo, D. Cash, K. Mellodew, S.C. Williams, S.E. Fraser, T.J. Meade, J. Price, H. Hodges, Tracking transplanted stem cell migration using bifunctional, contrast agent-enhanced, magnetic resonance imaging, Neuroimage 17 (2002) 803–811.
[45] A.S. Arbab, G.T. Yocum, H. Kalish, E.K. Jordan, S.A. Anderson, A.Y. Khakoo, E.J. Read, J.A. Frank, Efficient magnetic cell labeling with protamine sulfate complexed to ferumoxides for cellular MRI, Blood 104 (2004) 1217–1223.
[46] M. Babic, D. Horak, M. Trchova, P. Jendelova, K. Glogarova, P. Lesny, V. Herynek, M. Hajek, E. Sykova, Poly(L-lysine)-modified iron oxide nanoparticles for stem cell labeling, Bioconjug. Chem. 19 (2008) 740–750.
[47] J. Yang, J. Liu, G. Niu, K.C. Chan, R. Wang, Y. Liu, E.X. Wu, *In vivo* MRI of endogenous stem/progenitor cell migration from subventricular zone in normal and injured developing brains, Neuroimage 48 (2009) 319–328.
[48] K. Baeten, P. Adriaensens, J. Hendriks, E. Theunissen, J. Gelan, N. Hellings, P. Stinissen, Tracking of myelin-reactive T cells in experimental autoimmune encephalomyelitis (EAE) animals using small particles of iron oxide and MRI, NMR Biomed. 23 (2010) 601–609.
[49] E.M. Shapiro, S. Skrtic, K. Sharer, J.M. Hill, C.E. Dunbar, A.P. Koretsky, MRI detection of single particles for cellular imaging, Proc. Natl. Acad. Sci. U. S. A. 101 (2004) 10901–10906.

Clinical Cancer Research

Tissue redox activity as a hallmark of carcinogenesis: from early to terminal stages of cancer

Rumiana Bakalova, Zhivko Zhelev, Ichio Aoki, et al.

Clin Cancer Res Published OnlineFirst March 26, 2013.

Author Manuscript Published OnlineFirst on March 26, 2013; DOI: 10.1158/1078-0432.CCR-12-3726
Author manuscripts have been peer reviewed and accepted for publication but have not yet been edited.

Tissue redox activity as a hallmark of carcinogenesis: from early to terminal stages of cancer

Rumiana Bakalova,[1,2] Zhivko Zhelev,[1,3] Ichio Aoki,[1] Tsuneo Saga[1]

[1]Diagnostic Imaging Program, Molecular Imaging Center, National Institute of Radiological Sciences (NIRS), 4-9-1 Anagawa, Inage-ku, Chiba 263-8555, Japan
[2]Medical Faculty, Sofia University "St. Kliment Ohridski", 1 Koziak Str., Sofia 1407, Bulgaria
[3]Medical Faculty, Trakia University, 11 Armeiska Str., Stara Zagora, Bulgaria

Running title: Tissue redox activity as a hallmark of carcinogenesis

Translational relevance

This study directly relates to cancer diagnosis, the assessment of cancer progression (from early to terminal stage) and planning a therapeutic strategy. This study demonstrates that tissue redox balance is very sensitive to cancer development and can be used as a diagnostic marker of carcinogenesis. The method is simple and applicable on isolated tissue and blood specimens. The method demonstrates the potential for promising application in molecular imaging diagnostic *in vivo* on humans following the development of cell-penetrating nitroxide probes with high contrast, low toxicity and minimal side effects.

The most important observations are that the oxidative status of noncancerous tissues (even those distant from the primary tumor locus) increases with cancer progression and that these tissues become susceptible to oxidative stress and damage.

Abstract

***Purpose*:** The study aimed to clarify the dynamics of tissue redox activity (TRA) in cancer progression and assess the importance of this parameter for therapeutic strategies.
***Experimental design*:** The experiments were conducted on brain tissues of neuroblastoma-bearing, glioma-bearing and healthy mice. TRA was visualized *in vivo* by nitroxide-enhanced magnetic resonance imaging (MRI) on anesthetized animals or *in vitro* by electron paramagnetic resonance (EPR) spectroscopy on isolated tissue specimens. Two biochemical parameters were analyzed in parallel: tissue total antioxidant capacity (TTAC) and plasma levels of matrix metalloproteinases (MMPs).
***Results*:** In the early stage of cancer, the brain tissues were characterized by a shorter-lived MRI signal than that from healthy brains (indicating a higher reducing activity for the nitroxide radical), which was accompanied by an enhancement of TTAC and MMP9 plasma levels. In the terminal stage of cancer, tissues in both hemispheres were characterized by a longer-lived MRI signal than in healthy brains (indicating a high oxidative activity) that was accompanied by a decrease in TTAC and an increase in the MMP2/MMP9 plasma levels. Cancer progression also affected the redox potential of tissues distant from the primary tumor locus (liver and lung). Their oxidative status increased in both stages of cancer.
***Conclusions*:** The study demonstrates that tissue redox balance is very sensitive to the progression of cancer and can be used as a diagnostic marker of carcinogenesis. The study also suggests that the noncancerous tissues of a cancer-bearing organism are susceptible to oxidative damage and should be considered a therapeutic target.

Key words: cancer, tissue redox activity, total antioxidant capacity, metalloproteinases, magnetic resonance imaging